LOW-TEMPERATURE STM STUDY AND MANIPULATION OF SINGLE ATOMS AND NANOSTRUCTURES

Doctoral Dissertation
Jožef Stefan International Postgraduate School
Ljubljana, Slovenia, August 2010

Supervisor: *prof. dr. Albert Prodan*

Co-supervisor: *ass. prof. Miha Škarabot*

Evaluation Board:

prof. dr. Igor Muševič, Chairman, Institut "Jožef Stefan", Ljubljana

prof. dr. Albert Prodan, Member, Institut "Jožef Stefan", Ljubljana

dr. Stefan Fölsch, Member, Paul-Drude-Institut für Festkörperelektronik, Berlin

Erik Zupanič

Low-temperature STM study and manipulation of single atoms and nanostructures

Doctoral Dissertation

Preučevanje in manipulacija posameznih atomov in nanostruktur z nizkotemperaturnim VTM

Doktorska disertacija

Supervisor: prof. dr. Albert Prodan

Co-Supervisor: ass. prof. dr. Miha Škarabot

August 2010

MEDNARODNA PODIPLOMSKA ŠOLA JOŽEFA STEFANA
JOŽEF STEFAN INTERNATIONAL POSTGRADUATE SCHOOL
Ljubljana, Slovenia

Index

Abstract

The theory behind scanning tunneling microscopy and spectroscopy is presented and the basic manipulation techniques are described. Construction details of a low-temperature scanning tunneling microscope for single atom manipulation experiments are given. Single crystal copper (111) and (211) surfaces are studied. Single atom extraction, followed by lateral manipulation procedures is demonstrated. Cobalt adatoms are deposited onto copper samples at room- and at low- temperatures. Cobalt nanoislands are observed and the Kondo effect on single cobalt adatoms is measured by means of scanning tunneling spectroscopy. A detailed study of the surface diffusion of cobalt adatoms as a function of temperature is presented. Embedded defects in the copper (111) surfaces are studied and their influence on the stability and properties of cobalt adatoms. It is shown by density functional theory calculations and proved by a deposition experiment that the embedded defects are substitutional silver atoms. The structure of cobalt pairs is studied into detail using a combination of manipulation and imaging techniques.

Povzetek

Predstavljeno je teoretsko ozadje vrstične tunelske mikroskopije in spektroskopije ter opisane so osnove različnih tehnik manipuliranja. Podane so konstrukcijske podrobnosti nizkotemperaturnega vrstičnega tunelskega mikroskopa za izvajanje eksperimentov s posameznimi atomi. Preučevane so bile površine monokristalov bakra s kristalografsko orientacijo (111) in (211). Demonstriran je proces izvlečenja atomov iz površine in njihova manipulacija v različne nanostrukture. Naprševanje kobaltovih atomov je bilo izvedeno na vzorce bakra pri sobni ter pri nizkih temperaturah. Z vrstično tunelsko spektroskopijo so bili preučevani kobaltovi nano-otoki ter opazovan Kondo efekt na posameznik kobaltovih atomih na površinah. Predstavljena je podrobna študija površinske difuzije kobaltovih atomov v odvisnosti od temperature. Opisani so v površino bakra orientacije (111) vgrajeni defekti, njihove lastnosti in njihov vpliv na stabilnost kobaltovih atomov. S pomočjo računov na osnovi teorije gostotnih funkcionalov in dodatno eksperimentalno potrjeno z dodatnimi naparevanji srebra na bakrove površine je bilo potrjeno, da ti defekti dejansko predstavljajo substitucijske atome srebra. Podrobno je bila preučevana tudi zgradba kobaltovih parov s kombinacijo tehnik slikanja in manipuliranja.

Abbrevations

A/D	=	analog to digital
AC	=	alternative current
AES	=	auger electron spectroscopy
D/A	=	digital to analog
DC	=	direct current
DFT	=	density functional theory
DOS	=	density of states
fcc	=	face-centered cubic
FWHM	=	full-width at half-maximum
GGA	=	generalized gradient approximation
IETS	=	inelastic electron tunneling spectroscopy
LDOS	=	local density of states
LEED	=	low energy electron diffraction
LGA	=	local density approximation
LHe	=	liquid helium
LN2	=	liquid nitrogen
LT	=	low temperature
ML	=	monolayer
PSD	=	phase-sensitive detector
PWSCF	=	plane-wave self-consistent field
RT	=	room temperature
SEM	=	scanning electron microscopy
SNOM	=	scanning near-field optical microscopy
SPM	=	scanning probe microscopy
STM	=	scanning tunneling microscopy
STS	=	scanning tunneling spectroscopy
TEM	=	transmission electron microscopy
UHV	=	ultra high vacuum

1 Introduction

As electronic devices become increasingly smaller, there is a strong need for understanding the physical and chemical properties of matter on a nanometer scale. Over 20 years after the visionary talk "There is plenty of room at the bottom" [1] by Richard P. Feynman the scanning tunneling microscope (STM) was invented. With the application of the STM a new era in nanometer-scale science and technology started.

STM operation is based on a quantum-mechanical effect called the electron tunneling. In case of STM this means that the electrical current flows through the vacuum between the metallic tip and the conductive or semiconductive sample if the separation between the two is small enough. The resulting tunneling current is a function of the tip-sample distance, the applied tunneling voltage, and the local density of states (LDOS) of the tip and the sample. An image of the sample surface is acquired by monitoring the tunneling current as the tip scans across the material. Although atomic resolution can be routinely achieved with a good STM at room temperature (RT), the advantages of low-temperature (LT) STM were soon recognized. Cooling the sample and the STM to cryogenic temperatures results in improved tunneling stability, it enables studies of specific low temperature phenomena and guaranties sufficient energy resolution for spectroscopy measurements. Thermally assisted diffusion of surface atoms and adsorbates is in addition completely suppressed at low enough temperatures.

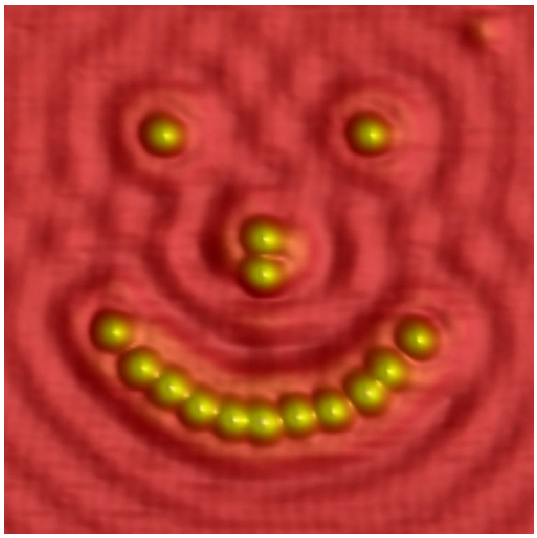

Figure 1: LT-STM image of individually manipulated Cu adatoms on Cu(111) surface. Area size $14 \times 14\,\mathrm{nm}^2$, $I_T = 1.0\,\mathrm{nA}$, $U_T = 100\,\mathrm{mV}$, $T = 8\,\mathrm{K}$.

With LT-STM it is possible not only to visualize surfaces with atomic resolution, but also to manipulate individual building blocks of matter into nanostructures and to probe local properties with high spatial and energy resolution. The sharp tip of the STM microscope can be used to perform lateral and vertical manipulation of adsorbed species, and to form and break individual chemical bonds. By arranging the building blocks of matter in a controlled way one can synthesize different chemical substances, dramatically increase the density of information storage and probe quantum phenomena. Finally, STM can be used to perform spectroscopy of single atoms and molecules on the surfaces studied.

As part of this dissertation an ultra-high vacuum (UHV) LT-STM, capable of single atom imaging and manipulation, was constructed. It was used to get a closer insight into the atomic scale manipula-

tion mechanisms and to investigate properties and stability of artificially constructed nanostructures. High purity Cu single crystals with atomically clean and flat surfaces were prepared and used as substrates. Individual Cu atoms were extracted from the sample surface with controlled tip-sample interaction. Co adatoms were deposited at RT and in-situ at LT. Isolated adatoms were then manipulated and arranged into different nanostructures. Diffusion and stability of the adsorbates were studied at different temperatures, with the special emphasis on the influence of naturally occurring embedded defects in the substrate onto Co adatom stability. The effect of embedded impurities onto the exchange coupling between single magnetic impurities and the conductive electrons of the metal host was measured. With the use of extensive density functional theory (DFT) calculations and with additional deposition experiments, the defects were identified as Ag substitutional atoms. Our observation of enhanced stability of the Co adatoms above Ag impurities suggests the exciting possibility of using embedded defects as templates for building artificial atomic structures, which would remain stable at elevated temperatures. Furthermore, our results indicate that ordered surface alloys might support self-assembly of magnetic impurity lattices.

The thesis is devided as follows. Introductory Chapter 1 deals with the purpose and the goals of this dissertation. The details of STM and STS are explained in Chapter 2. Chapter 3 gives an insight into the construction of the LT-STM, STM tip preparation and testing of the microscope. Chapter 4 explains the details of Cu single crystal surface preparation and of deposition of Cu and Co adatoms. In chapter 5 the results of adatom diffusion measurements are given followed by a study of Co adatom pinning by the embedded defects. Final conclusions are given in chapter 6.

2 Scanning tunneling microscopy and spectroscopy

Scanning probe microscopy (SPM) [2] is a precise surface method where images of surfaces are formed by a physical probe that scans across the sample. The probe is being mechanically displaced in a raster scan, line by line, and the image is recorded by measuring the probe-surface interactions as a function of the position. Most commonly used techniques are scanning tunneling microscopy (STM) [3], atomic force microscopy (AFM) [4] and scanning near-field optical microscopy (SNOM) [5].

The general principle of operation of a STM is surprisingly simple. It requires bringing a sharp STM tip close to the sample surface and applying a (mV to V) voltage difference between the two. This results in small (few pA to few nA) tunneling currents. The measured tunneling current is a function of the local density of states (LDOS) of the sample, the applied voltage and the distance between the tip and the surface. The topographic image of the sample surface is acquired by scanning the STM tip over the sample surface at a constant height or at constant current and recording the resulting tunneling current or the tip-sample distance.

Soon after the idea of the STM was proposed in 1982 [6] by G. Binning, H. Rohrer, C. Gerber and E. Weibel, the capability of the STM to image metal surfaces with atomic resolution was demonstrated [3]. Imaging and resolving the famous 7 x 7 Si (111) surface reconstruction [7] was the first great success of this new and powerful tool. Later efforts have been made to use STM to modify materials on the smallest possible scale. The possibility to locally pin molecules to a surface [8] and to transfer an atom from the STM tip to the surface [9] was successfully realized while the first experiment to show atom-by-atom construction of artificial nanostructures was performed in 1990 by D. M. Eigler and E. K. Schweizer [10]. Using a LT-STM they were able to position individual Xe atoms on a Ni (110) surface with atomic-scale precision. In 2000, S.-W. Hla et al. synthesized a single biphenyl molecule from two iodobenzenes [11]. With the LT-STM manipulation techniques they induced the Ullmann reaction on a Cu(111) surface by realizing basic reaction steps: dissociation, diffusion and association. Recently LT-STM was used to synthesise a linear metal-ligand complex from individual atoms and organic molecules deposited on an ultrathin insulating film [12]. Few atomic layers thick insulating films were employed to electronically decouple individual molecules from the metallic substrate. This e.g. allowed direct probing of the unperturbed molecular orbitals [13, 14]. By using a magnetic tip STM can be made sensitive to the spins of the tunneling electrons [15]. Using spin-polarized (SP) STM allows resolving different spin structures at the atomic level, as well as imaging and even manipulating the spin direction of individual atoms [16].

In addition to the ability to provide high-resolution topographic information, one of the most important features of STM is that the images also contain data related to the local electronic structure of the surfaces or of the adsorbates on the surfaces. This was already observed as voltage-dependent changes in the appearance of Si (111) 7 x 7 surface reconstruction [7]. Compared to other surface spectroscopy techniques such as X-ray photoemission spectroscopy (XPS), ultraviolet photoemission spectroscopy (UPS) and Auger electron spectroscopy (AES), which all average over a large surface region [17], STM has the unique advantage of obtaining spectroscopic information with atomic spatial resolution[1].

Building artificial atomic-scale structures, probing local quantum phenomena, studying properties of single atoms and molecules, inducing single molecule reactions and studying reaction mechanisms at a fundamental level makes STM one of the most important modern nanotechnological tools.

There is a number of comprehensive books on STM microscopy [2, 18–21] and review papers on selected topics such as tunneling theory [22, 23], high resolution image interpretation [24, 25],

[1] For a sharp STM tip the tunneling current is confined laterally to a radius of a few tenths of a nanometer.

interaction of two-dimensional electrons with surface nanostructures [26,27], imaging of metal surfaces [28], direct observation of spin structures [29], time-resolved STM [30], studying of high-temperature superconductors [31], chemical identification via inelastic tunneling spectroscopy [32,33], manipulation of single molecules [34] and atoms [35] and single-molecule chemistry [36–38].

2.1 Theory of scanning tunneling microscopy

When a sharp metal tip is brought within close proximity of a sample surface, so that their wave functions overlap, a finite probability exists that electrons will cross the energy barrier between them. Although forbidden in terms of classical physics but already observed in 1960's in planar junctions [39], an electrical current will be detected in case if a bias voltage is applied across the junction. A real space topographic image of the sample surface is acquired by recording the variation in the tip-sample distance needed to keep the tunneling current constant during line-by-line scanning of the STM tip (Figure 2a).

The system can be simplified by assuming the one-dimensional case, where the sample as well as the tip are described by an ideal metal with electron states filled up to the Fermi energy E_F. The two metal electrodes are separated by a small vacuum gap d and an applied negative tunneling voltage V_T will shift the Fermi energy of the tip by eV_T. Φ_s and Φ_t are the work functions of the sample and the tip, respectively (Figure 2b).

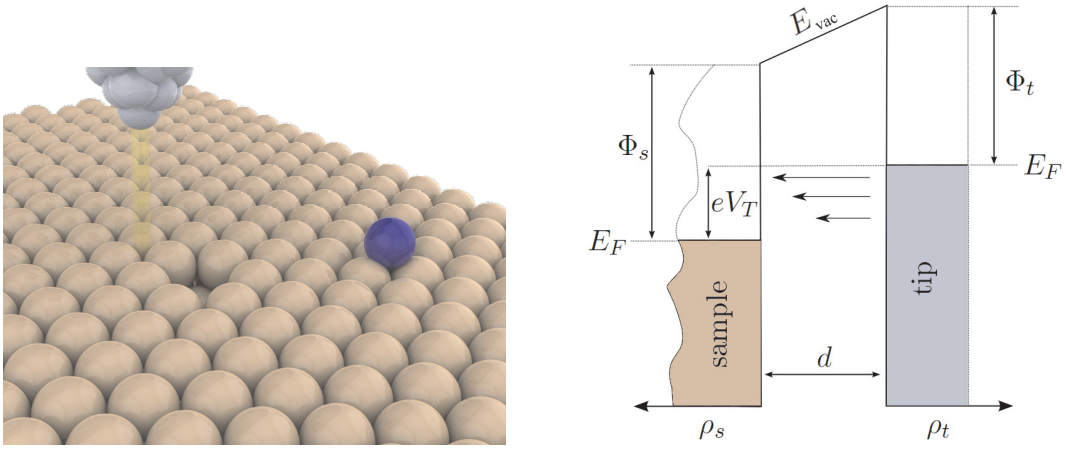

(a) (b)

Figure 2: (a) Schematic representation of the tunneling junction. An atomically sharp metal STM tip is being scanned over the sample surface, keeping the distance and thus the tunneling current constant. The image is formed by recording movement of the tip. (b) When a negative bias voltage is applied to the STM tip the Fermi level E_F raises by eV_T and the electrons from occupied states of the tip (right-hand side) will tunnel into the unoccupied sample states (left-hand side). Therefore they must overcome a trapezoidal energy barrier formed by the work functions of the sample Φ_s, the tip Φ_t and eV_T.

An electron, represented by its wavefunction $\psi(d)$, has a finite probability to be found in the barrier region or in the sample at the position d:

$$\left|\psi(d)\right|^2 = \left|\psi(0)\right|^2 e^{-2kd}, \quad k = \sqrt{\frac{m_0}{\hbar^2}(\Phi_t + \Phi_s - eV_T)}. \tag{2.1}$$

Since most workfunctions are of the order of 4-5 eV 2k will typically be about 20 nm^{-1}, which means that a variation in d of 0.1 nm results in an order of magnitude difference in the tunneling probability. This relationship between the tunneling current and the tip-sample distance is the reason for the extremely high vertical resolution of the STM, which can easily reach the sub-picometer range. On the other hand, electron tunneling can in practice only be observed for very small separations. Keeping the current even moderately stable requires extreme STM tip positional control, limiting mechanical vibrations and electrical noise to the lowest possible level.

When a small bias V_T is applied, only electronic states near the Fermi level (within E_F and $E_F + eV_T$) are excited and tunnel across the vacuum barrier. The process requires that there is an empty level on the other side of the barrier, of the same energy as the one of the tunneling electron. By introducing the concept of the local density of states (LDOS) $\rho(d, E)$ one can express the tunneling current from the tip to the sample as [40]:

$$I_{t\to s} = \frac{4\pi e}{\hbar} \int_{-\infty}^{\infty} \rho_t(\epsilon - eV_T)\rho_s(\epsilon) f_t(\epsilon - eV_T)(1 - f_s(\epsilon)) \left|M(\epsilon - eV_T, \epsilon)\right|^2 d\epsilon, \tag{2.2}$$

where ρ_s and ρ_t are the LDOS of the sample and the tip, $f(\epsilon) = (1+exp[\epsilon/k_BT])^{-1}$ the temperature dependent Fermi-Dirac distribution for the electrons, and $M(\epsilon_t, \epsilon_s)$ the tunneling matrix element which describes the interaction of the electron wavefunctions in the tip with those in the sample.

After summation of the tunneling currents in both directions, from the tip to the sample and vice-versa, the total tunneling current can be written as:

$$I_T = \frac{4\pi e}{\hbar} \int_{-\infty}^{\infty} \rho_t(\epsilon - eV_T)\rho_s(\epsilon)(f_t(\epsilon - eV_T) - f_s(\epsilon)) \left|M(\epsilon - eV_T, \epsilon)\right|^2 d\epsilon, \tag{2.3}$$

The equation for tunneling current is quite simple but the real difficulty represents evaluation of the tunneling matrix element M. In the one-dimensional simplification M is given by:

$$\left|M(\epsilon - eV_T, \epsilon)\right|^2 \;=\; exp\Big[-2z\sqrt{\frac{m_e}{\hbar^2}(\Phi_t + \Phi_s - eV_T + 2\epsilon)}\,\Big]. \tag{2.4}$$

Determining the matrix element in a more realistic approximation is almost impossible since the actual geometry and the chemical structure of the tip are generally not known.

An ideal STM tip would consist of a point source of the tunneling current, which would result in a best possible resolution and in no tip-surface interaction. In such a case the STM would measure the LDOS of the bare surface around the Fermi level. Using the first-order perturbation theory [41] J. Tersoff and D. R. Hamann gave an analytical expression for the matrix element [42,43], solving the problem for an atomically sharp tip, where only the atom closest to the sample surface contributes to the tunneling current. The wavefunction of this atom is described by a spherical, s-like orbital and the DOS over the energy interval of interest is assumed to be constant.

The equation (2.3) can be rewritten using the Tersoff-Hamann tunneling matrix in the form:

$$I_T \;=\; \frac{16\pi^3 C^2 \hbar^3 e}{k^2 m_e^2}\rho_t \int_{E_F}^{E_F+eV_T} \rho_s(\epsilon)d\epsilon. \tag{2.5}$$

The parameter C is a constant and k is given as in equation (2.1). In this approximation the tunneling current can be considered as proportional to the DOS of the sample, integrated across the $(E_F, E_F + eV_T)$ energy window.

2.2 Imaging

Imaging of a conductive or semiconductive sample surface can be performed either in the constant-current or the constant-height mode. In both cases the tunneling (bias) voltage is set constant while the STM tip is being scanned line-by-line over the sample surface. The motion of the atomically sharp tip in all three directions (X, Y and Z) is controlled by piezoelectric elements (the technical details of STM are described in Chapter 3).

In the constant-current mode (Figure 3a) the tunneling current is set and held constant by a feedback mechanism, which controls the tip-sample distance d during scanning. The recorded changes in the distance (i.e. vertical movement of the tip) give a real-space image of the sample surface, or rather the constant LDOS of the surface. Altering the tunneling current or the bias voltage results

in different tip-sample distances and produces different LDOS contours. Depending on the polarity of V_T, occupied or unoccupied states near the E_F in the sample are recorded [44].

When imaging in the constant-height mode (Figure 3b), the applied bias voltage and the tip-sample distance are set constant, while the image is formed by recording the tunneling current during scanning. The changes in surface topography will alter the tip-sample distance and thus the recorded current. This mode is usually used to image relatively smooth surfaces as otherwise a tip might crash into the sample surface. The advantage of this mode is that it can be used at high scanning frequencies (up to 200 Hz) [45] because the system doesn't require an adjustment of the tip-sample separation.

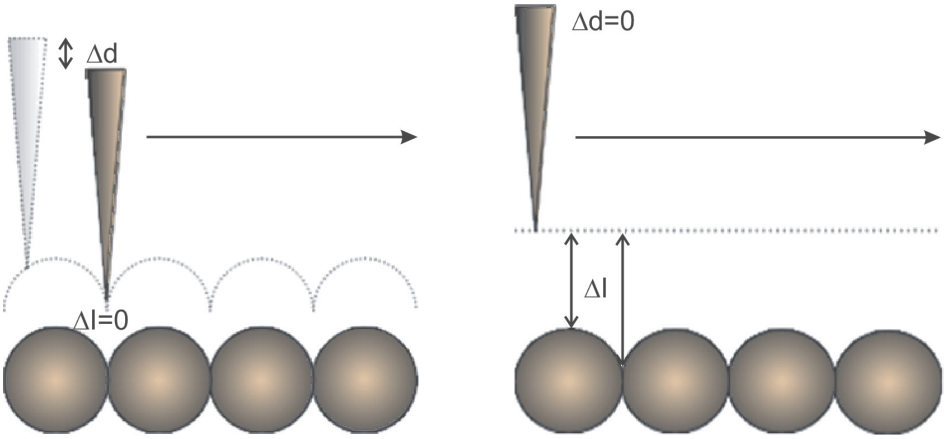

Figure 3: The principle of the STM operation in constant-current (a) and constant-height (b) imaging modes.

It is obvious from (2.5) that the tunneling current is always a function of the tip-sample distance and the LDOS of the sample under the STM tip. Therefore the acquired STM images are always a convolution of the surface topography and the local electronic structure of the sample. Interpretation of the STM data is therefore not always straightforward [46]. The sample LDOS can be affected e.g. by surface state modulations and point defects.

Atomic resolution imaging can be routinely achieved with STM. The vertical resolution largely depends on the stability of the tip-sample distance and is typically below 10 pm, while the lateral resolution is limited by the geometry of the scanning tip and the sample and by their respective electronic structures. For example, the large corrugation amplitudes obtained in the constant-current STM images of close packed metal surfaces are still not fully understood [47–49].

2.3 Spectroscopy

Scanning tunneling spectroscopy (STS) gives information on the local electronic structure and allows one to study electronic properties of individual (ad)atoms [50], molecules [51], clusters (i.e. C60 [52]) and semiconductor quantum dots [53]. There are three modes of spectroscopy measurements used: i) I-d [54], where a variation of the tunneling current I_T, which depends on the tip-sample distance d, is measured at a constant bias voltage V_T, ii) V-d [55], where I_T is kept constant and the variation in d is measured as a function of V_T, and iii) I-V [56], where z is kept constant and I_T is measured as a function of V_T. Additionally, inelastic processes, where the energy is no longer conserved during electron tunneling between the tip and the sample, can be directly measured with the inelastic electron tunneling spectroscopy (IETS) [51, 56–60].

If the energy eV_T is small compared to the work functions of the tip and the sample and if the tunneling matrix element M in equation (2.3) is assumed constant, the tunneling current can be written as:

$$I_T \propto \int_{-\infty}^{\infty} \rho_t(\epsilon - eV_T)\rho_s(\epsilon)(f_t(\epsilon - eV_T) - f_s(\epsilon))d\epsilon, \tag{2.6}$$

Calculating the first derivative of the tunneling current I_T with respect to the bias voltage V_T, assuming a constant LDOS of the tip and keeping the tunneling junction at zero temperature, we get:

$$\left.\frac{dI_T}{dV_T}\right|_{V_T} \propto \rho_t \int_{-\infty}^{\infty} \rho_s(\epsilon)\delta(\epsilon - eV_T)d\epsilon = \rho_t\rho_s(eV_T). \tag{2.7}$$

Thus, the derivative dI_T/dV_T is in general a good approximation to the LDOS of the sample at the energy value eV_T. The I-V STS measurements are performed by first bringing the STM tip into the required position and by setting the desired tip-sample distance by adjusting the tunneling voltage and the tunneling current. Then the feedback loop is opened, which keeps the distance d constant. The tunneling current is then recorded while ramping the voltage over the desired range. The changes in the slope of the obtained I-V curve reflect variations in the conductance of the tip-sample junction. The tunneling current is usually too noisy to obtain reliable data, thus the dI/dV signal is directly measured with the help of the Lock-In technique.

2.3.1 The Lock-In technique

To obtain high signal-to-noise ratio spectroscopy curves, a small high-frequency sinusoidal signal $V_m sin(\omega t)$ is superimposed onto the constant DC tunneling voltage. This modulation causes a sinusoidal response in the tunneling current (Figure 4a), which can be expanded into a Taylor series:

$$I(V_T + V_m sin(\omega t)) \approx I(V_T) + \frac{dI(V_T)}{dV} V_m sin(\omega t) + \frac{dI^2(V_T)}{dV^2} V_m^2 sin^2(\omega t) + ... \tag{2.8}$$

By extracting the first harmonic frequency we obtain a signal, which is proportional to the differential conductivity dI/dV and therefore to the LDOS of the sample.

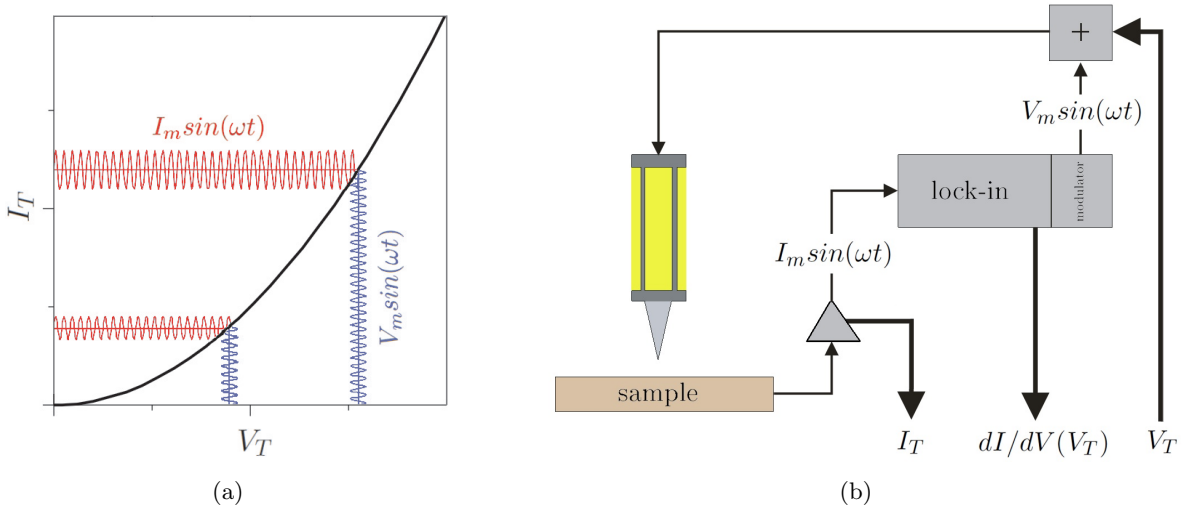

Figure 4: (a) A small modulation of the tunneling voltage (blue) results in a modulated tunneling current (red). The amplitude depends on the slope of the I-V curve. (b) A schematic presentation of the experimental setup for STS measurements with the lock-in amplifier.

A phase-sensitive detector (PSD) in a lock-in amplifier multiplies the input V_{input} (i.e. tunneling current) with a reference signal V_{ref}, taken from the internal oscillator and phase shifted by φ. The resulting output V_{PSD1} is a DC signal, where only the in-phase current of the same frequency as the reference contributes to the output (Figure 4b). The phase dependency can be eliminated by using a lock-in with two PSDs. The second PSD multiplies the input with a reference signal, shifted by 90 degrees. By computing the magnitude $R = \sqrt{V_{PSD1}^2 + V_{PSD2}^2}$ the phase dependency is removed.

The resolution of the STS measurements is largely dominated by the broadening caused by the voltage modulation and by the finite temperature of the system [61, 62]. The measured dI/dV signal is a convolution of the LDOS of the sample and an *instrumentation function* ϕ of the lock-in. For

example, as shown in Figure 5b a perfectly constant LDOS with a delta function at a certain energy (Figure 5a) is broadened into a peak with a width of 2 eV_m and a FWHM of 1.22 eV_m. A similar effect is expected because of a finite temperature, where broadening of the delta function results in a peak with FWHM of 3.2 k_BT (Figure 5c). At the ambient temperature of $T = 300$ K, the energy resolution is limited to $\Delta E \approx 80$ meV, while at 7 K the resolution of the measurements is strongly enhanced to $\Delta E \approx 2$ meV.

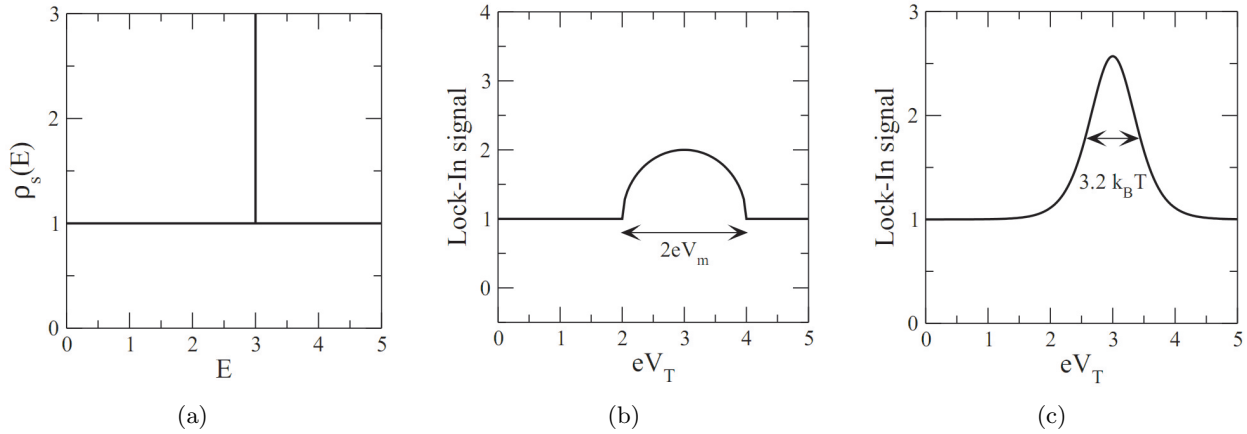

Figure 5: The STS resolution is limited by the temperature and by the modulation broadening. A delta function LDOS (a), is broadened into a peak with a width of 2 eV_m due to modulation broadening (b) or into a peak with FWHM of 3.2 k_BT (c) due to thermal broadening. Figure reproduced from [61].

As mentioned before, the high spatial resolution of STM is used for extremely local measurements of the sample DOS. It is also possible to map the LDOS of a certain surface area at a defined energy. This is performed by slowly imaging the surface in the constant-current mode while simultaneously modulating the applied tunneling voltage V_T and at the same time detecting the dI/dV signal[2]. The result of spatially resolved STS mapping is a plot of LDOS of the scanned area at the energy eV_T and represents a powerful and discerning means for studying e.g. electron scattering [63].

2.4 Manipulation

There are different kinds of manipulation techniques possible with the STM tip. For example, it is possible to precisely position individual atoms and molecules on surfaces [9, 10, 12, 64–74], induce motion [75–85] or even modify the chemistry of a single molecule [11,12,86–88]. To induce manipulation one must control different processes between the tip and the adsorbate: attractive and repulsive short-range atomic forces, inelastic excitations by tunneling electrons or tip-induced electric field forces.

2.4.1 Lateral manipulation

If an STM tip is positioned very close to the adsorbate, short-range atomic forces are established, which can relocate single atoms or even molecules across the sample surface. The procedure, known as *lateral manipulation* typically involves three steps: i) reduction of the distance between the tip and the manipulated adsorbate, thereby increasing the tip-adsorbate interaction, ii) displacement of the tip laterally to the desired final position and iii) retraction of the tip back to the scanning distance (Figure 6).

By recording the tip height (current) signal during the lateral manipulation process in constant current (constant height) mode, one can precisely track the adsorbate motion on the sample surface and study the tip-adsorbate interactions involved. [67,89,90] Three different basic lateral manipulation modes, *pulling*, *sliding* and *pushing*, can be distinguished (Figure 7).

[2]The modulating frequency is typically much higher than the cut-off frequency of the feedback loop response and is thus not interfering with the tip control.

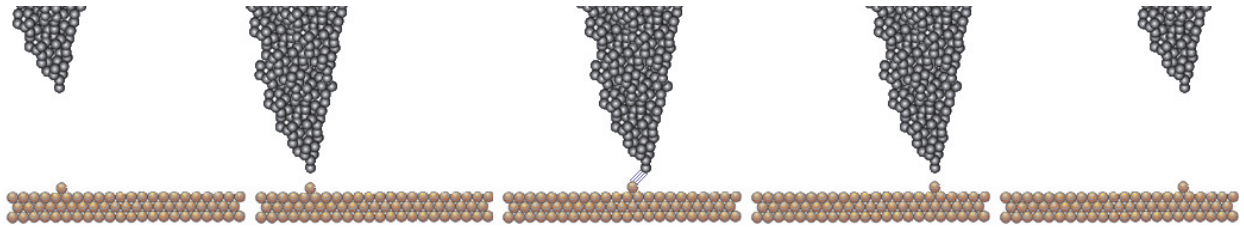

Figure 6: Schematic illustration of the lateral manipulation process. First, the STM tip is positioned above the selected adsorbate and is lowered from the scanning into the manipulation distance, second, the attractive forces between the adatom and the tip become strong enough for the adatom to follow the movement of the tip and finally, after the displacement the tip is retracted to the scanning distance.

In the *pulling* mode the adsorbate follows discontinuously the motion of the tip due to an attractive force. When the lateral force component overcomes the hopping barrier of the adsorbate, the atom/molecule jumps to the next adsorption site under the tip, causing (in case of constant current mode manipulation) an abrupt increase in the height signal (Figure 7a). The periodicity of the signal corresponds to the distance between the neighboring adsorption sites. By further reducing the tip-adsorbate distance and thus by increasing the interaction, an adsorbate can be manipulated in a continuous, *sliding* mode. The adatom[3] is trapped under the tip and the height signal corresponds to the surface corrugation (Figure 7b). During the *pushing* manipulation mode, the adatom is pushed by the STM tip due to the repulsive forces between the tip and the adsorbate. The tip height increases as the tip approaches the adsorbate and then suddenly decreases as the adatom jumps to the next adsorption site (Figure 7c).

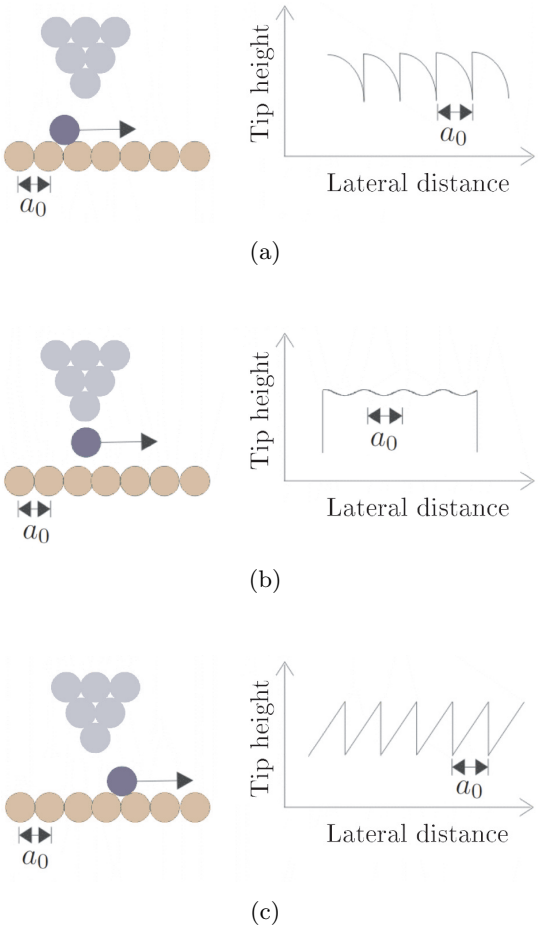

Figure 7: Illustration of the pulling (a), sliding (b) and pushing (c) modes of lateral manipulation procedures. The characteristic STM signals during manipulation are shown on the right of the respective illustrations.

[3]An adatom is an atom that is adsorbed on a surface.

2.4.2 Vertical manipulation

During the lateral manipulation, the contact between the adsorbate and the surface is never lost. In case of the *vertical manipulation* mode it is possible to transfer atoms/molecules reversibly between the STM tip and the substrate surface [91, 92]. The adsorbate transfer process can be realized by means of a tip-adsorbate physical contact, by using the electric field between the tip and the adsorbate or by excitations via inelastic tunneling of the electrons.

The inelastic electron tunneling transfer mechanism can be explained with a double potential well model [93]. The transfer of the adsorbate can be regarded as a potential-barrier crossing problem between two potential wells, formed by the interaction of the adsorbate with the STM tip and the sample. The inelastic tunneling electrons loose their energy and excite vibrational levels of the adsorbate-sample bond.

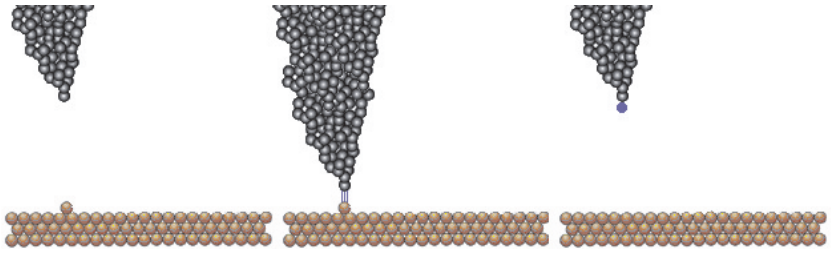

(a)

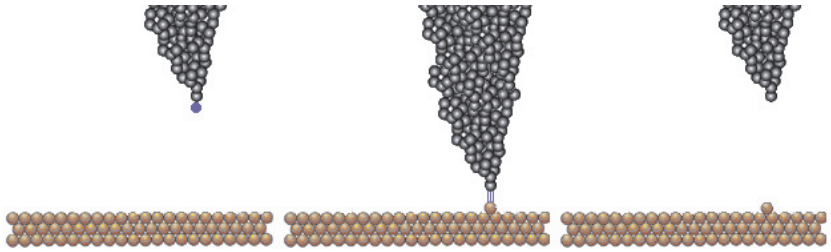

(b)

Figure 8: The vertical manipulation process enables reversible transfers of adsorbates between the STM tip and the surface. The procedure involves the transfer of an adsorbate onto the STM tip (a), the displacement of the STM tip with the adsorbate and the deposition of the adsorbate back onto the sample surface (b).

The vertical manipulation process can also be used to modify the STM-tip. The tip sharpness can be improved (and thus the image resolution) by attaching an atom or a molecule onto the tip apex. Tips with attached molecules are used in chemical contrast imaging when, for example, a CO molecule on the STM tip enables distinction between adsorbed CO molecules and O atoms on a metal surface [92].

2.4.3 Manipulation induced by inelastic excitations

Controlled manipulation can be induced by means of inelastic electron tunneling. In this case tunneling electrons (or holes, dependent on the polarity of the tunneling voltage) are injected into the adsorbate located under the STM tip. Their energy is transferred to the vibrational modes of the atom or a molecule through the adsorbate induced resonance state, leading to different excitations. During this process the energy of the tunneling electrons is controlled by the tunneling pulsed voltage, and the excitation rate by the tunneling current [36]. Namely, the number of tunneling electrons passing through the adsorbate depends on the tunneling current and hence on the variation in the excitation rate: $R \propto I^N$, where R is the dissociation rate, I the tunneling current and N the number of electrons involved in the process.

By using inelastic electron tunneling rotational, vibrational and electronic excitations can be induced [37] and chemical bonds can be broken and formed [11]. Due to highly localized tunneling electrons, modifications of individual selected bonds inside a single molecule are possible.

Figure 9 shows a sequence of step-by-step single molecule manipulation, where iodine was separated from iodobenzene, the two resulting phenyls were brought together by means of lateral manipulation, and finally they were chemically bonded into a biphenyl molecule.

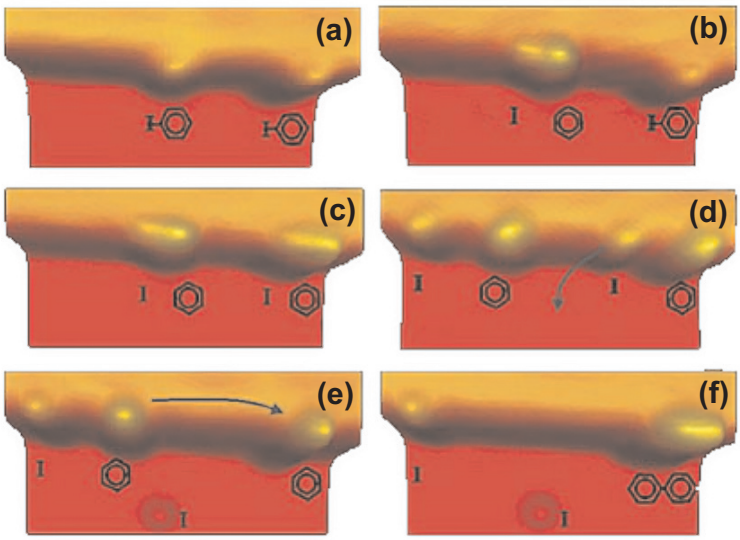

Figure 9: STM images showing individual steps of a single molecule Ullmann reaction. (a) Two iodobenzene molecules are adsorbed on a Cu(111) step edge and the iodines are removed from the phenyl rings by using voltage pulses (b,c). By means of a lateral manipulation the two resulting molecules are brought together (d,e) and chemically associated into a biphenyl molecule (f). Figures reproduced from [11].

2.4.4 Manipulation induced by electric field

An electric field is induced when a tunneling voltage is applied between the STM tip and the underlaying substrate. Due to the small separation distance between the two electrodes the strength of this electric field is very high even at low tunneling voltages[4]. Figure 10 shows a simulated electric field between a STM tip, modeled as a sphere, and a planar metallic surface, with a potential difference of 3V. In practice, the exact shape of the field is not known because of the unknown geometric structure of the tip.

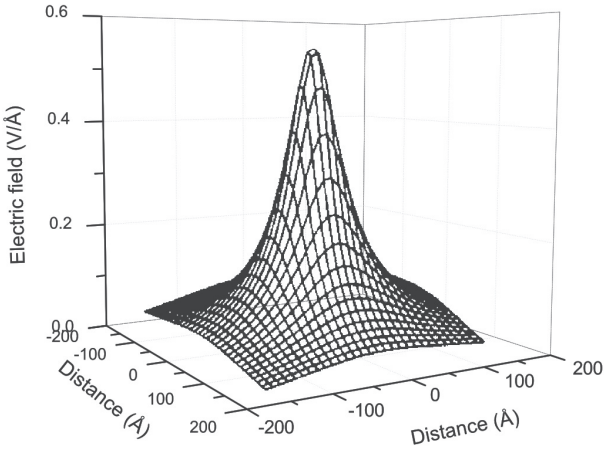

Figure 10: Calculated electric field for a potential of 3V and a separation distance of 5 Å (reproduced from [64]). The electric field has a peak strength of 0.6 V/Å or 6 x 10^9 V/m.

An atom or a molecule having a dipole can experience attractive or repulsive forces from this electric field and can be laterally manipulated across the surface [94, 95]. At higher tunneling voltages (i.e. at

[4] A tunneling voltage of 100 mV and an estimated separation distance of 0.5 nm result in an electric field of 0.2 x 10^9 V/m.

stronger electric fields) molecular bonds can be broken [96]. When the applied voltage overcomes the value of the work function of the tip or the surface, the electrons are field emitted.

3 Construction of the experimental set-up

The STM and STS experiments presented in this thesis were performed with a home-build UHV LT-STM system (Figure 11). An existing RT-STM Omicron STM-1 instrument was complemented with a liquid-helium (LHe) cooled LT-STM. A Besocke beetle type STM scanner is in thermal contact with a liquid helium bath cryostat. The working temperature of the instrument is 7 K and the base pressure inside the system is in the low 10^{-10} hPa region. The microscope offers high stability and low thermal drifts, which allows high resolution imaging and low noise spectroscopy measurements.

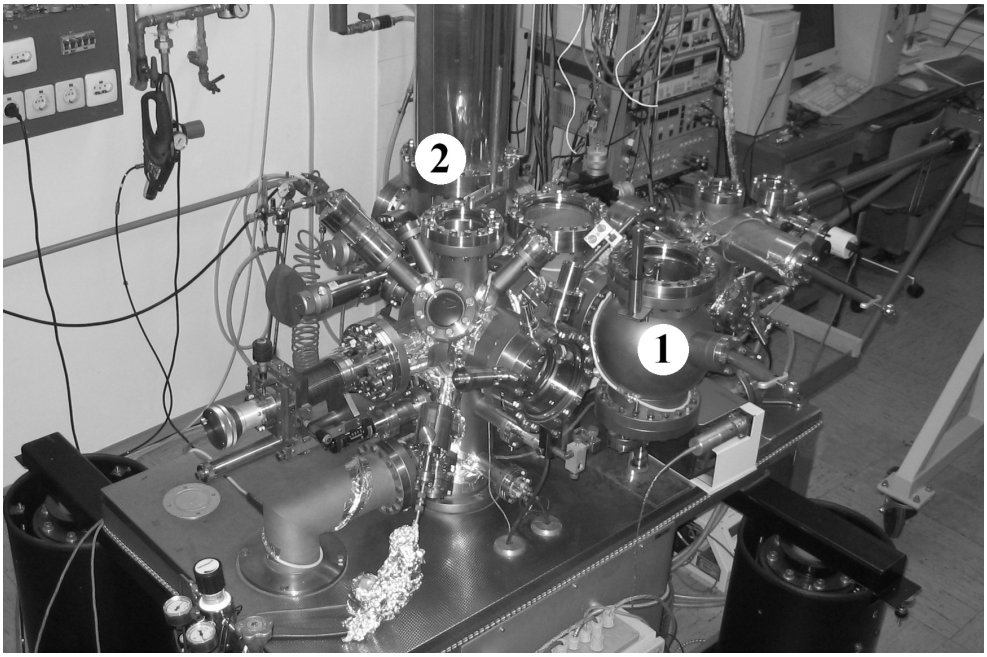

Figure 11: The ultra-high vacuum system with the room-temperature (1) and the low-temperature (2) STM, with additional other equipment for sample preparation and characterization.

3.1 The UHV system

The use of UHV (pressure below 10^{-9} hPa) is essential for the preparation and atomic-resolution imaging of atomically clean surfaces, which would otherwise be contaminated during the time scale of an experiment. A roughly estimated time to cover a surface with a monolayer of contaminants at 10^{-6} hPa is about a second, while at UHV conditions the sample surface will stay clean for days. The actual rate of contamination at a certain background pressure and temperature depends upon the nature of the surface[1]. Only with the development of all-metal gasket seals in 1962, reliable means for achieving UHV conditions became available [97].

Reaching UHV conditions can be quite challenging and requires [98]:

- use of UHV pumps, i.e. ion pumps, titanium sublimation pumps, cryopumps,
- use of clean UHV compatible materials (low outgassing and low vapor pressure materials), i.e. metals, special ceramics, glass, teflon,

[1]The *sticking coefficient* S is a measure of surface reactivity and is in the range of 0 to 1.

- use of special seals and gaskets,
- minimization of the surface area,
- avoiding pits of trapped gas - virtual leaks,
- usage of short and high cross-section tubing,
- baking of the UHV system to remove water and other surface contaminants.

The experimental system consists of six interconnected UHV chambers schematically shown in Figure 12. The samples are loaded into the system through a load lock chamber and are transferred through UHV by means of a magnetic linear manipulator and three wobble-sticks. The preparation chamber is equipped with a VSW AS10-C sputter Ar^+ ion gun and a home-made radiation heating stage for sample annealing. The sample storage chamber is the central part of the UHV system, from where the samples are transferred to the LT-STM chamber, to the Omicron STM-1 RT-STM chamber or to the analysis chamber, equipped with an Omicron SpectraLEED combined low-energy electron diffraction (LEED) and Auger electron spectrometer (AES). The system is additionally equipped with a Balzers QMG112A quadrupole mass spectrometer and an Omicron EFM3 Knudsen source. To reduce vibrations transferring from the environment to the STM chamber, the entire vacuum system is suspended on Melles Griot 07OTI033 pneumatic vibration isolators, which provide both vertical and horizontal isolation.

Figure 12: Schematic representation of the UHV system, consisting of a LT-STM chamber (green), a RT-STM chamber (yellow), a cryostat (blue), a sample storage chamber (gray), an analysis chamber (cyan), a preparation chamber (magenta) and a load lock (red).

The system is continuously pumped by two Varian Starcell ion pumps (125 l/s and 20 l/s) and periodically by a titanium sublimation pump, while two rotary and two turbo pumps are operated only during bake-out procedures. The system is baked at a relatively low temperature of 110 °C; this temperature was chosen to prevent softening and desintegration of the glue used to assemble the LT-STM scanner. A single infrared fan is used for heating and a special ironing fabric cover for thermal isolation during bake-out periods.

3.1.1 The cryostat

Cooling a LT-STM to cryogenic temperatures is usually done either by LHe bath cryostats [99] or by LHe flow cryostats [100, 101]. Our LHe bath cryostat (Figure 13) made by the Cryotechnic group, is based on the original design of G. Meyer [99]. It consists of a 4 l LHe reservoir, encircled by a larger 5.3 l liquid nitrogen (LN2) shroud whose main purpose is to reduce losses via radiation transfer from the vacuum chamber walls (at RT) to the helium cooled part of the cryostat. To additionally lower the LHe consumption there is a thermal link from the top of the LN2 reservoir to the upper part of the LHe neck, which provides heat sinking to the LN2 temperature; the temperature gradient on the longer portion of the neck is thus significantly smaller. Additionally, a number of radiation plates (baffles) are soldered to the LHe neck to reduce radiation losses in the vertical direction. The STM head is suspended by three stainless-steel springs from the copper plate at the bottom of the LHe reservoir and damped by eddy currents. This results in a good mechanical vibration isolation but also in a weak thermal contact to the LHe reservoir. The head is surrounded by two pairs of thermal radiation shields, made of gold-plated copper, one pair in good thermal contact to the LHe tank and the other pair to the LN2 tank. These shields are used to thermally isolate the cooled STM head from the warm environment. Each pair consists of a static (inner) part and a rotating (outer) part. Rotating radiation shields (shutters) allow sample transferring into and from of the STM and permit an optical access to the STM scanner. The shutters are operated by means of a rotary feed-through, and are cooled by copper braided wires that link the rotating shields with the LHe and LN2 tanks. Special care was taken to reduce any openings in the radiation shields as the radiation losses are one of the main limiting factors for both the ultimate working temperature and the LHe consumption [102, 103].

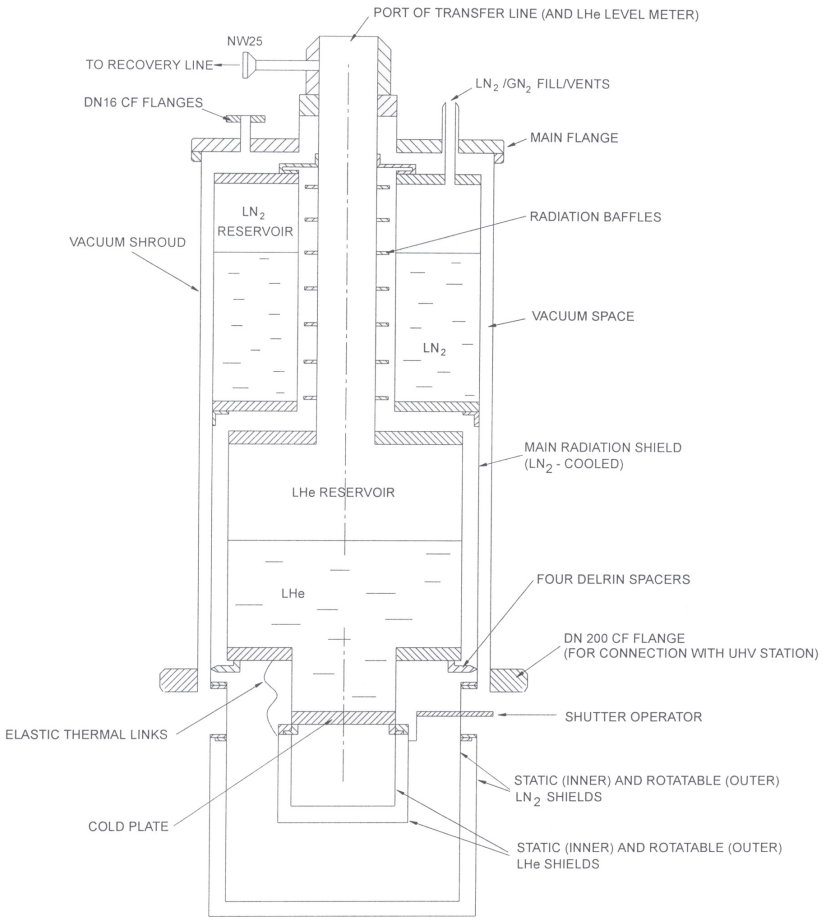

Figure 13: A schematic drawing of the LHe bath cryostat, used to cool the LT-STM head. The main components are indicated.

The hold times of the cryostat are 14 h for LN2 and 26 h for LHe (provided the LN2 reservoir is never empty); thus continuous measurements can only be performed for 14 hours. The working

temperature of the STM is 7.0 K and is measured under the sample holder. A rotating feed-through mechanism is used to pull the STM head into contact with the cooling plate at the bottom of the static LHe radiation shield. The cooling-down time for the STM from RT to LN2 temperature is approximately 30 h, and it takes further 24 h to reach the lowest attainable temperature.

3.1.2 The LT-STM head

A Besocke beetle type STM head [104,105] was chosen for our LT-STM. The scanner head is compact and well known for its inherent high mechanical stability and good drift compensation [106]. Besocke scanners allow scanning of the sample surface, approaching the STM tip towards the sample from a macroscopic distance to the tunneling conditions as well as positioning the tip relative to the sample. Main parts for our modified head were purchased from Createc GmbH. To retain compatibility with the existing RT microscope the new LT-STM head was modified to accept the Omicron sample plates.

The main components of the STM head are the four piezoelectric tubes (Staveley Sensors EBL #2, PZT-5A) with a metal coating sectioned longitudinally into four quadrants on the outside and a single continuous electrode on the inside wall [107–109]. A circular copper plate called *the beetle* rests on the three outer tubes with sapphire balls. The fourth piezoelectric tube with the scanning tip is mounted at the center of the beetle (Figure 14a). The movements of the beetle are achieved with the three outer tubes by means of the inertial sliding technique. Small cycles of stick and slip movements of the ring relative to the tubes are performed by applying a suitable sawtooth wave form voltage. The tubes are driven laterally by applying bipolar symmetric voltages on opposite segments of the outer electrodes, while the tubes are extended or shortened by applying the same voltage on all four outer electrodes. For lateral movements all tubes are displaced in the same direction while the rotation of the beetle is achieved by driving all three tubes tangentially (see Figure 14b). Since the beetle has three ramps on the bottom side, this rotation is accompanied by a vertical movement and is used for the coarse approach of the tip towards the sample surface.

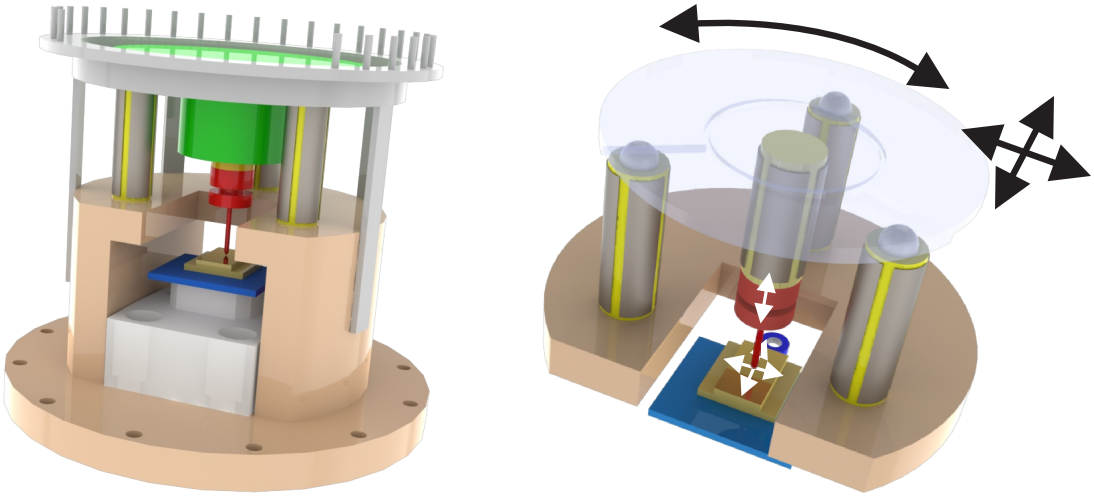

(a) (b)

Figure 14: a) A model of the modified Besocke LT-STM head. The STM tip (red) is approached to the sample surface (gold) by rotating a circular Cu plate (green) with three outer piezoelectric tubes (yellow-grey). (b) Rotation or lateral movement of the Cu ring (black arrows) is achieved by three outer piezo tubes, while the scanning (white arrows) is usually performed with the fourth, central piezo tube.

A high-voltage amplifier from Createc, based on Apex PA85 MOSFET amplifiers is used to generate signals, which drive the piezoelectric tubes. The amplitude and the frequency of this driving signals have to be carefully chosen, depending on the temperatures at which the system is operated[2].

The STM tip holder is attached to the central piezo tube by means of a magnet and the Omicron

[2]The piezoconstants are temperature dependent and are in case of lateral movements approximately 50 Å/V at 7 K and 77 Å/V at 80 K.

sample holder is clamped into place by two stainless steel springs, coated with TiC for low friction. The temperature is measured under the sample holder with a LakeShore DT471 Si diode.

The piezo tubes are glued to the gold coated copper part with a special UHV compatible two-component epoxy patch EP-1 from Caburn MDC. The glue is very strong and has a very low degassing rate, but can only withstand bake-out temperatures up to 125 °C; at higher temperatures it becomes softer.

The wires used to connect the STM head piezo tubes and the temperature diode with the intermediate connector on the bottom of the LHe reservoir are polyamide-insulated 75 μm and 100 μm diameter constantan (0.45Ni-0.55Cu) wires from the California Fine Wire Company. Thin flexible wires are used to prevent transmission of any vibrations from the cryostat to the STM head. The wires used to connect the intermediate connector (cooled to LHe temperature) with the UHV electric feed-through (at RT) are from stainless-steel, 150 μm in diameter and polyamide insulated. These were chosen for their low heat conductivity and high mechanical strength. A coaxial wire is used for the tunneling current and the tunneling voltage and is wired separately from the high-voltage signals used to drive the piezo tubes. All wires were soldered using lead-free silver-tin alloy Castolin 157 in conjunction with the Castolin 157N liquid flux. The flux is etching and has to be carefully removed to avoid short circuits. All signal wires must be properly thermally anchored, ether by gluing them or by mechanically pressing them against cold surfaces, or by using beryllium oxide heat sink blocks.

The assembled LT-STM head and the Omicron sample holder are shown in Figure 15.

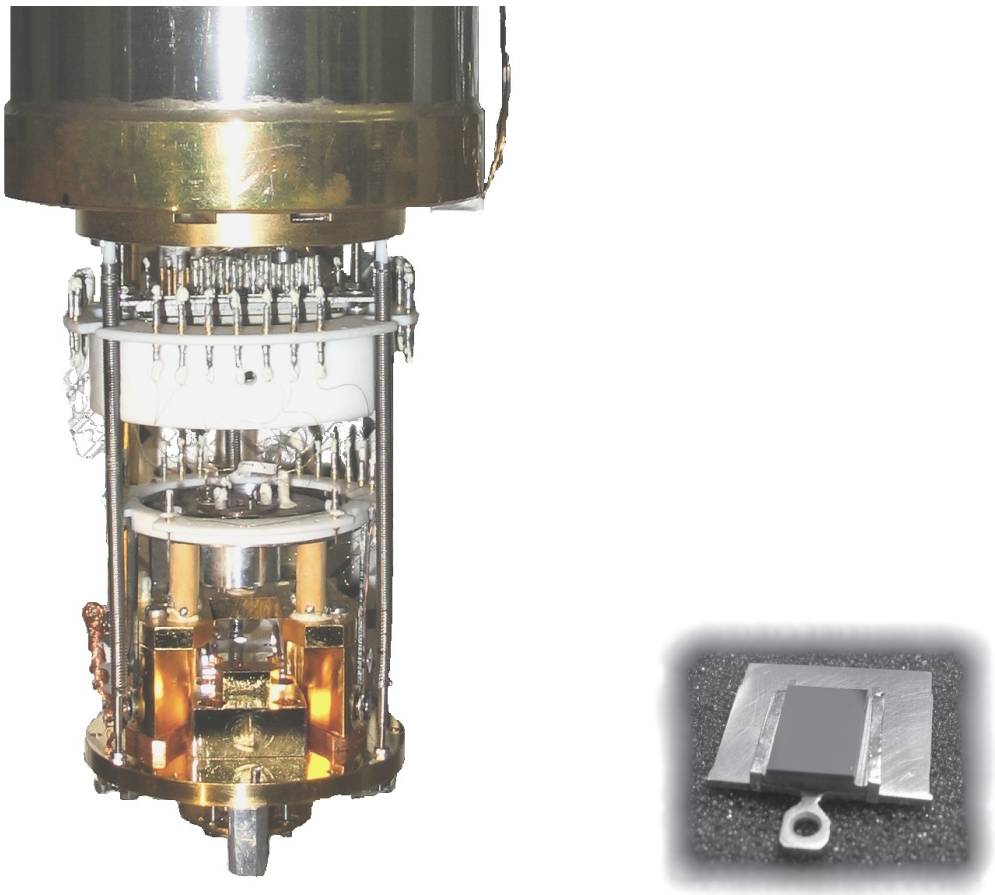

(a) (b)

Figure 15: a) The modified LT-STM head under the LHe cryostat and (b) the Omicron sample holder with a polished sample attached by two Ta foil stripes.

A mechanical feed-through mechanism is used to pull the STM head into mechanical (and thermal) contact with the bottom of the LHe reservoir, allowing faster cooling and providing mechanical stability needed when sample holders are interchanged. Due to a weak thermal contact of the free hanging STM head to the LHe reservoir (i.e. during scanning), additional 200 μm diameter Au wires were used

to thermally couple the head to the reservoir. This shortens significantly the cooling time and reduces the working temperature, but on the other hand introduces new pathways to transfer vibrations from the cryostat to the STM. The wires had to be later removed since they caused additional vibrations.

3.2 Electronics and the software

The electronics from Createc GmbH allows a digital control of the Besocke type LT-STM head. A digital signal processor (DSP) is connected to the analog electronics (a high voltage amplifier and a tunneling current preamplifier) by four 20 Bit digital-to-analog (D/A) and four 18 bit analog-to-digital (A/D) converters. It controls the scanning and the feedback loop of the STM (Figure 16a). Three D/A converters are used to control the piezo voltages, while the fourth converter is used for the bias voltage (between -10 and +10 V). One A/D converter is used to read the amplified tunneling current while the others are used to record other signals (e.g. dI/dV from an external lock-in amplifier).

The bipolar three-channel high-voltage amplifier has an independently selectable gain for each channel (1x, 3x, 10x or 30x) and a maximum output voltage of 200 V. The amplifier has a bandwidth of 60 KHz.

The tunneling current preamplifier (I/V-converter) is a Femto DLPCA2000 with a gain between 10^3 and 10^{11} V/A. The bandwidth depends on the selected gain and ranges from 1.1 KHz to 500 KHz.

External cables must be properly shielded to prevent picking up high-frequency electromagnetic interferences from the environment. A correct grounding of the cables and the electronics is thus essential [110]. Shields of the cables should be grounded at one point only, grounding loops have to be avoided and high-quality cables are to be used. It is also important to connect the current preamplifier as close to the tunneling junction as possible to reduce electromagnetic interferences in the tunneling signal. This is done by connecting it directly to the BNC feed-through at the top of the cryostat. We also found that powering the STM electronics through an insulation transformer significantly reduces the electrical noise.

For spectroscopy measurements we use a Stanford SR830 digital lock-in amplifier, whose integrated modulator is used as a source for modulating tunneling voltages. Since the minimum output voltage amplitude is 4 mV, we used a simple 1:10 voltage divider to reduce the modulating voltage by a factor of 10. The modulating voltage frequency was set to 670 Hz.

The STM software is running on a PC with the Windows operating system (Figure 16b). The program allows standard data acquisition, data analysis, different spectroscopy measurements, lateral and vertical manipulation in different modes, tip forming and 3D image rendering.

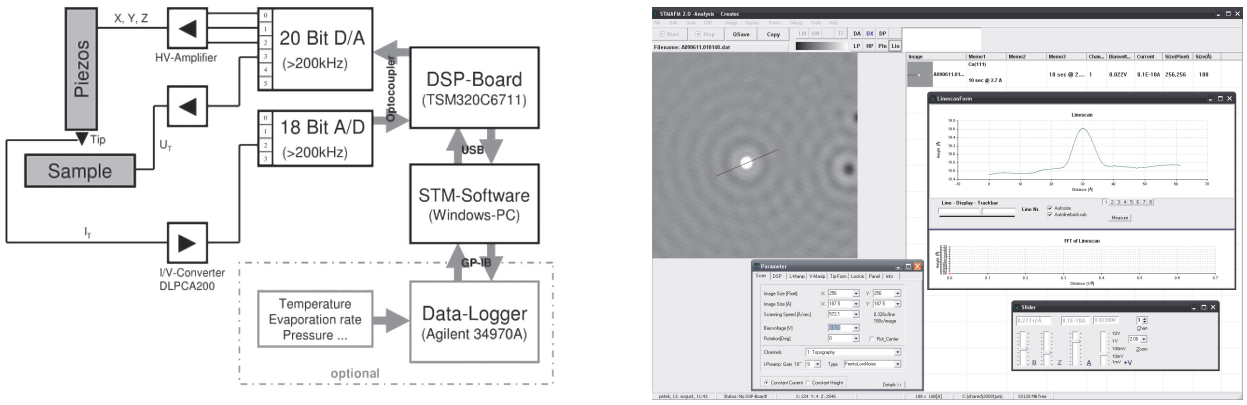

(a) (b)

Figure 16: (a) The STM electronics and (b) the program used for STM and STS measurements and data analysis.

The recorded images were analyzed and processed with the WSxM program [111]. To show up features of interest in some low corrugation STM images, removal of the low-frequency noise by means of a low-pass filter, flattening and contrast enhancement were necessary.

3.3 Tip and sample preparation

Sharp, stable and clean tips are essential for the described work. There is a number of materials used and numerous recipes were suggested for the preparation of STM tips [112–114].

Etched W tips are usually used [115–117]. Their production is based on electrochemical etching in KOH and NaOH solutions under an AC or DC current, which allows an excellent control of the tip shape and size at the apex. The tips can be made very sharp and stable due to their hardness, and they can be in-situ cleaned and also reconditioned by dipping them in a controlled way into the sample surface. This procedure makes them ideal for UHV STM experiments, although they can also be used in air [118] and electrochemical environments [119]. However, their lifetime in air is limited because of their oxidation [120]. Pt/Ir tips are often used in air since they are inert and oxide free, but they are not suitable for highly corrugated surfaces. They are usually made by cutting a wire with scissors, which does not allow a proper preparation control. Etching of Pt/Ir tips is possible in CN solutions but due to possible toxic hazards the method is not widely used [113]. An alternative method is the use of a concentrated NaCl solution at high AC voltages.

All measurements presented in this thesis were performed with electrochemically etched W tips. An annealed W wire of 99.95 % purity with a diameter of 0.375 mm was etched in a 2M KOH solution and controlled with a homebuild rapid-shutdown electronics. The typical response time of the electronic circuit is around 500 ns and the etching current can be manually set between 10 and 20 mA. The electronics is powered by a 12V battery to avoid electrical noise from the mains. The W wire is connected as the anode and a ring of a Au wire is used as a cathode. With an etching current of 10 mA the process takes about 10 minutes. The crucial point to obtain sharp tips is to cut off the etching current immediately after the wire drops off at the air-electrolyte interface [121]. After etching the tip is rinsed with deionized water and ethanol, and crimped into a tube of the tip holder. Care must be taken not to bend the tip apex during ultrasonic cleaning or to expose the tip to a jet of a liquid from the perpendicular direction. As-etched tips are always chemically contaminated with different thin carbonaceous phases and always coated with a layer of W oxide [120]. This contaminants are usually removed by a short (10 second) etching in concentrated HF shortly before the tip is introduced into the UHV system[3] [122]. The tips are usually additionally prepared in-situ by ion bombardment [123] or annealing [120], which was not possible to perform in our UHV system.

STM tips were characterized by optical microscopy and scanning electron microscopy (SEM) (Figure 17). While SEM does not distinguish a sharp tip from a blunt one, the very apex of the tip and even individual oxide layers can be studied by transmission electron microscopy (TEM) [124]. Usually field-emission from the tip apex is used to determine the effective apex curvature [124].

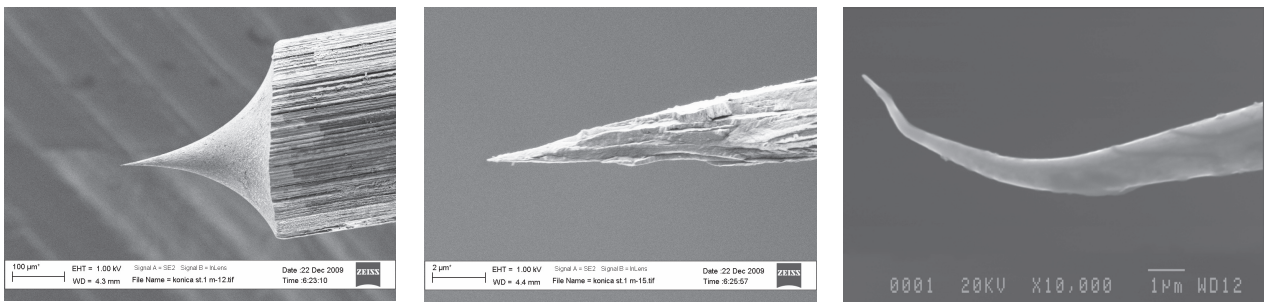

(a) (b) (c)

Figure 17: Low- (a) and high- (b) magnification SEM image of a sharp STM tip. Tip shown in (c) was bend during ultrasonic cleaning. All tips are electrochemically etched from a W wire.

The final and most important tip reconditioning is done by a controlled interaction of the STM tip with the soft metal substrate (such as Cu or Ag) [125]. Thus the tip apex is covered with sample atoms and its sharpness can be accordingly improved. Another technique to improve the tip apex is to use voltage pulses, which usually remove a few atoms/molecules only. One can also use a harsher

[3] All W oxides are soluble in concentrated HF, while W itself is not.

reconditioning procedure, where a high DC voltage (100 V) is applied to the tip, which is brought into contact with the sample surface. This is the first procedure we usually use when we start working with a new STM tip. It is worth mentioning that most experiments described in this thesis were performed with the same STM tip.

Experiments with UHV-STM usually require atomically flat surfaces with the same chemical composition as in the bulk of the sample. The in-situ sample preparation procedure involves surface cleaning with ion sputtering and smoothing by annealing procedures [126]. Ion sputtering is done by accelerating Ar^+ ions to 1 keV and bombarding the sample surface at a small angle. Sputtering disrupts the crystal lattice and the sample must be subsequently annealed. This involves a radiative heating of the back side of the sample holder with an ordinary light bulb. Since elevated sample temperatures also enhance diffusion of the contaminants from the bulk of the sample to its surface, ion sputtering needs to be repeated several times. After a few cleaning cycles the gradient of contaminant concentration is decreased in the subsurface region and the surface remains relatively clean[4].

The cleaning procedure was automated using an Oxford ITC4 temperature controller and a computer, which controls both, the annealing time and temperature and the accelerating voltage of the ion gun. During annealing the ion current is cut off (by setting the accelerating voltage to 0 V) and the emission current is reduced to improve the life-time of the ion gun thoriated-W cathode. The temperature of the sample is measured by means of a thermocouple, mounted to the holder of the annealing stage.

The surface composition and structure are checked with Auger electron spectroscopy (AES) [127] and low-energy electron diffraction (LEED) [128], respectively. In AES incident focused electrons with an energy of 3 keV knock out core-state bound electrons in the sample. The resulting holes are filled with electrons from higher energy (outer-shell) orbitals and the difference in energy is carried by a third electron (Auger electron), ejected from the atom. Because of the low energy of the emitted electrons (up to 3 keV), they have a short mean free path in a solid and the escape depth of electrons is only few atomic layers thick. This makes AES a surface sensitive method. The collected Auger electrons are analyzed and a diagram showing *derivative of the number of Auger electrons* as a function of *energy* is drawn. The weak point of our Omicron SpectraLEED was the integrated lock-in amplifier. With the use of an external Stanford SR8300 lock-in amplifier a much better energy resolution was achieved. Figure 18 shows AES spectra of a contaminated and of a sputtered Cu(111) sample.

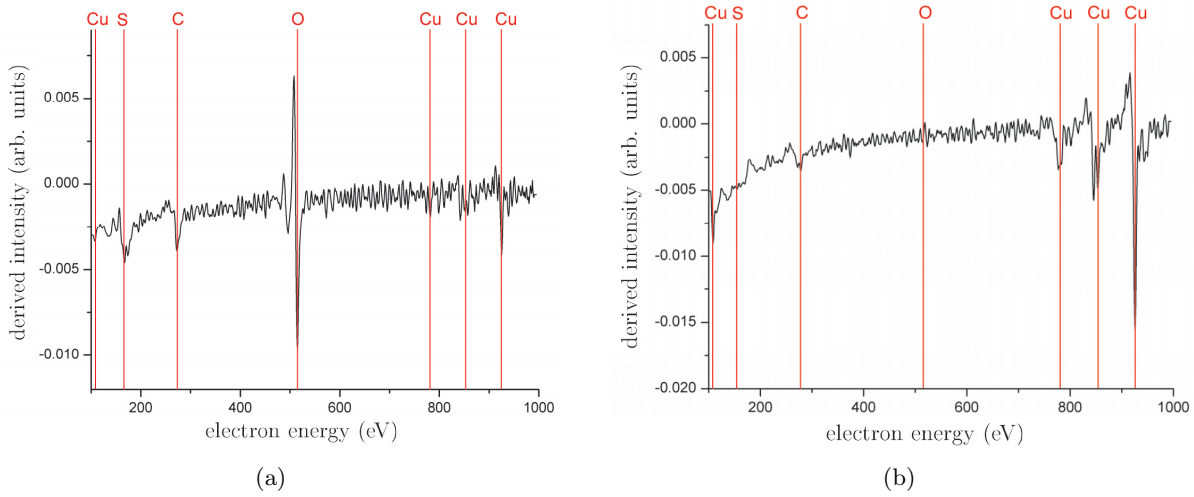

Figure 18: Unfiltered single-pass AES spectra of a contaminated (a) and a clean (b) Cu(111) surface. The contaminated surface is covered with a thick layer of oxides and carbides.

In LEED low energy electrons (typically up to 100 eV) are focused onto the sample surface. Due to the wave-nature of the electrons they are diffracted and elastically back-scattered onto a phosphorescent screen. The diffraction pattern gives information on the type of the crystal structure, while the sharpness of the diffraction peaks depends on the presence of the disorder. The strong

[4]Typically 5-10 cycles are needed to obtain clean and flat Cu(111) and (211) surfaces.

interaction of the low-energy electrons with the material is the main reason for the high surface sensitivity of LEED. Figure 19 shows LEED patterns of a contaminated and an in-situ cleaned Cu(111) surface. The diffraction pattern from the in-situ prepared sample indicates a well ordered and clean surface, suitable for STM experiments.

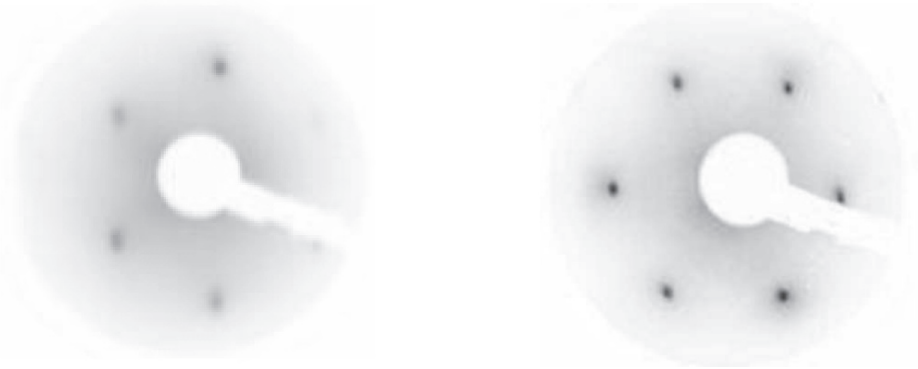

(a) (b)

Figure 19: LEED diffraction patterns, recorded on a contaminated Cu(111) surface (a) and on a well ordered and clean Cu(111) surface (b).

Deposition of submonolayer amounts of metal atoms is usually performed with UHV atom beam sources [129]. In a Knudsen source the electrons are emitted from a heated filament and accelerated towards a metal rod or a crucible, containing the metal or the molecules to be evaporated. When a determined vapor pressure of a heated substance is achieved, the vapors exit through a well-defined opening in the form of a directional beam of atoms or molecules. An Omicron EFM3 Knudsen source was used to deposit Co adatoms onto sample surfaces at RT, while resistive heating of a high purity Mo wire with Co wire wrapped around it was used to deposit Co in-situ onto cooled samples.

3.4 The performance

The performance of the LT-STM was tested on a Cu(111) surface with an electrochemically etched W tip. Figure 20a shows an unfiltered topographic constant-current STM image of a clean Cu(111) surface. Such images are used to calibrate the lateral piezo constants (the vertical constants are calibrated by measuring the heights of the surface steps).

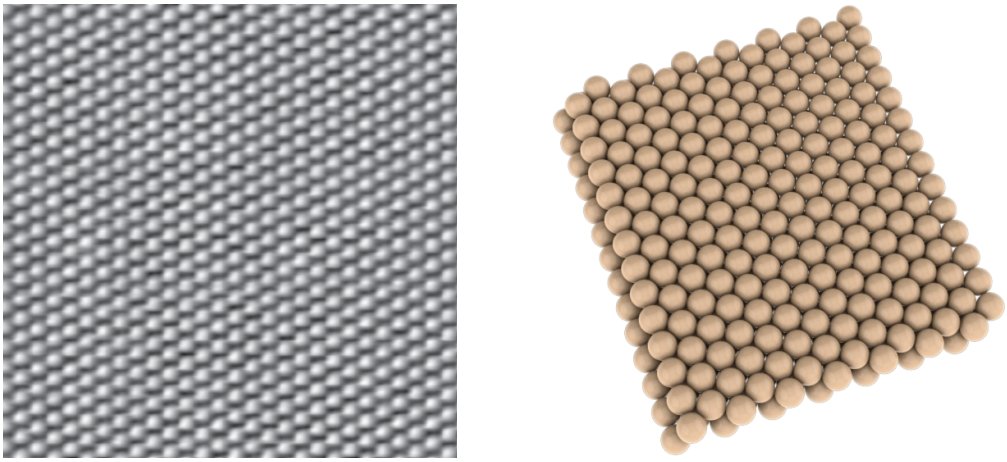

(a) (b)

Figure 20: (a) Atomic resolution LT-STM image of an ideal Cu(111) surface. Positions of individual atoms are clearly recognized. Area size $6.3 \times 6.3\,\mathrm{nm}^2$, $I_T = 2.0\,\mathrm{nA}$, $U_T = 50\,\mathrm{mV}$, $T = 8\,\mathrm{K}$. (b) A ball model of the close-packed fcc Cu(111) surface.

The performance of the LT-STM system was quantified by imaging the surface of a Cu(111) single crystal at lower magnifications and by calculating the standard deviation of the topographic signal along and perpendicular to the fast scanning direction. The standard deviation along the fast scanning direction equals $\sigma = 1.0$ pm and along slow scanning direction $\sigma = 2.0$ pm (Figure 21).

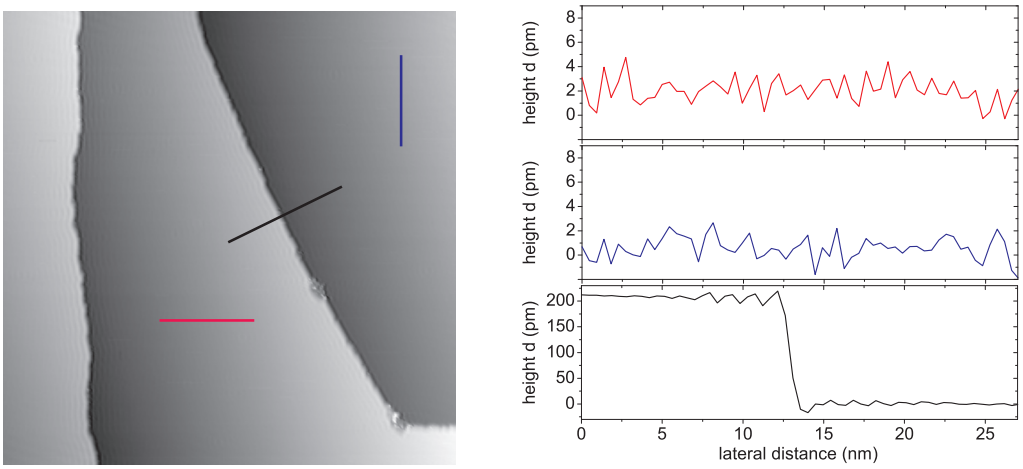

(a) (b)

Figure 21: (a) A topographic LT-STM image of a Cu(111) surface with terraces and single-atomic steps. Line profiles along the fast, the perpendicular to the fast scanning direction, and across a step-edge are plotted in (b). Area size $115 \times 115\,\mathrm{nm}^2$, $I_T = 0.8\,\mathrm{nA}$, $U_T = 111\,\mathrm{mV}$, $T = 8\,\mathrm{K}$.

The stability of the microscope and the energy resolution of the STS measurements were tested on Co adatoms on Cu(111) surfaces. Co adatoms represent magnetic impurities on a metallic substrate and show a Kondo effect, i.e. a spin flip scattering between a single magnetic atom and the electrons of the metal host. A sharp zero bias feature is detected in the spectroscopy curves, which is interpreted as the Kondo resonance [130]. A series of Fano line shaped dI/dV spectra was recorded, which show excellent reproducibility and high-energy resolution (Figure 22).

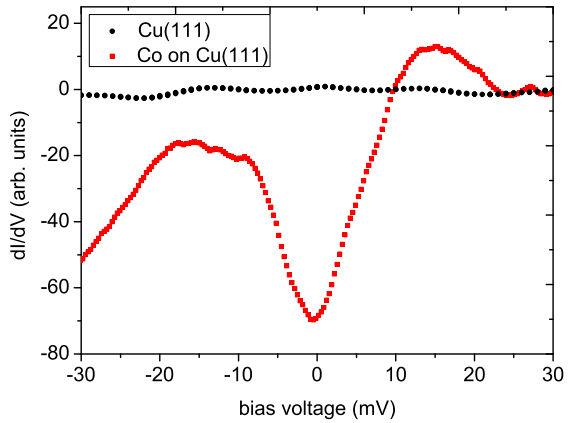

Figure 22: STS spectra recorded with the tip positioned above a clean Cu(111) surface (black) and above an isolated Co (red) adatom. The later shows a sharp dip around E_F, attributed to the negative Kondo resonance. Modulating voltage $V_m = 2\,\mathrm{mV}$.

In conclusion, a new UHV LT-STM, designed for single atom manipulation experiments was successfully constructed and tested. The modified Besocke-type scanning head can accept Omicron type sample holders. It is operated at 7K and is capable of achieving atomic resolution on low-corrugation nobel metal surfaces. The microscope offers high mechanical stability and can be used for high quality spectroscopic measurements.

4 Clean and adsorbate covered Cu(111) surfaces

Single crystal surfaces of noble metals were and still are intensively studied because of their importance as substrates in surface manipulation and restructuring experiments [131–133]. Noble-metal deposits on other noble-metals [134, 135] as well as deposits of magnetic metals on noble-metals [136–140] were intensively studied by scanning tunneling microscopy (STM) and related methods. Atomic and molecular adsorption on these substrates is likewise of great importance for catalysis. Such studies included adsorption of elements like H, O, N, S and C on Pt(111) [141] and N on Cu(001) [142], but also deposits of simple molecules like NO_2 on Ag(111) [143], SO_2 on Cu(110) [144] and CO on Ag(111) [145], Ag(221) [146] and Cu(111) [92, 147]. Further, STM was intensively employed to study the behavior of more complicated molecules on noble-metal surfaces [148–159] and to investigate heteroepitaxial growth of inorganic compounds, like MoO_3 on Au(111) [160]. Reverse combinations, i.e. deposits of noble-metals on layered inorganic compounds, mostly transition-metal dichalcogenides [161–163], with particular emphasis on postintercalation of the deposits into the van der Waals (vdW) gaps of the substrates [164] were also investigated. In last years intensive surface studies have been performed on thin metal oxide films on nobel metal substrates [165–167].

In this chapter, the study of the properties of Cu(111) and (211) single crystal surfaces is presented. We are particularly interested in structural aspects of the surfaces, like e.g. its stability during scanning, but also in the role of various surface defects, like point defects accompanied by electronic standing waves, which characterize these surfaces at reduced temperatures. Furthermore, extraction of individual Cu atoms and their manipulation into different arrangements is described and the ability of STS as a spectroscopic method is demonstrated in case of individual Cu adatoms on the Cu(111) surface.

4.1 Experimental details

High purity (99.9999 %) Cu single crystal surfaces with (111) and (211) orientations were purchased from the Surface preparation laboratory[1]. Electro-polished samples with the orientation accuracy below 0.5 degrees were mounted on Omicron stainless-steel sample holders by two Ta foil stripes, spot-welded onto the holder (Figure 14b). The sample surface was rinsed with pure isopropanol and blown with dry nitrogen. The sample holders were introduced into the UHV system, where they were cleaned during repeated (3 - 10) in-situ heating (T = 900 K, t = 5 min) and ion-beam etching (1 keV Ar^+ ions, I_{ion} = 5 μA, t = 20 min) cycles. The number of cycles depended on the condition of the sample surface. Initial cleaning of oxidized and heavily contaminated surfaces[2] was performed by several hours of ion sputtering. This not only removed the surface contamination but also the top layers of the bulk material. For the samples already cleaned in-situ and kept under UHV conditions, it was sufficient to perform a few cleaning cycles only. The parameters for the sputtering and the annealing cycles were optimized by controlling the crystallography and the chemistry of the surfaces by LEED and AES, respectively.

After cleaning the samples were either transferred directly into the precooled LT-STM or submonolayer amounts of Co atoms were first deposited onto the sample surface at RT, and then transferred into the precooled LT-STM. The temperature of the STM head raised substantially after the RT samples were introduced because of the high temperature difference and low thermal capacity of the head at cryogenic temperatures [103]. The rapid heating from 7 K to about 52 K in 30 minutes was

[1] SPL, Penningweg 69 F, The Netherlands.
[2] Usually the case with new samples.

followed by a slow cooling back to cryogenic temperatures and it took about 10 hours for the STM head to reach agian a stable, working temperature below 10 K (Figure 23).

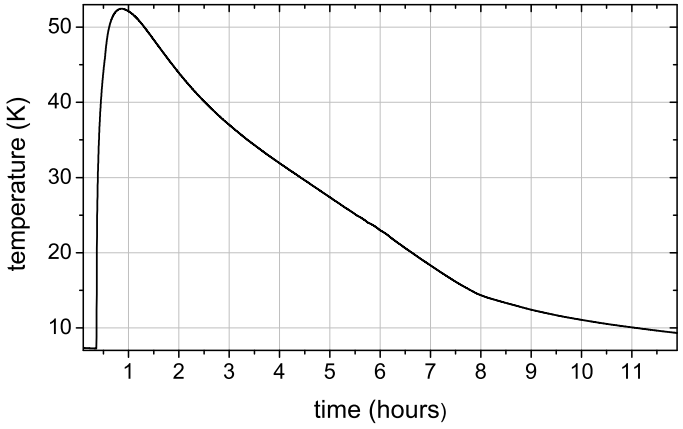

Figure 23: Sudden increase in the temperature of the precooled STM head after the introduction of a sample at room-temperature is followed by a slow cooling to the working temperature. It takes about 10 hours for the STM head with the sample to cool from 52 K to temperatures below 10 K.

STM constant-current measurements were performed close to the LHe temperature under UHV conditions ($p < 10^{-10}$ hPa). Differential conductivity dI_T/dV_T spectra were recorded at chosen surface positions with a digital lock-in amplifier (Stanford Research SR830). The tunneling voltage modulation frequency used was 670 Hz with an amplitude of 1 - 20 mV_{rms} was used. Higher modulation amplitudes yield better signal-to-noise ratios, which result in shorter acquisition times, but reduces the STS resolution (details are given in section 2.3.1). Tunneling voltages refer to the sample voltage with respect to the tip. An electrochemically etched W tip was used, routinely reconditioned by controlled tip-sample interaction.

4.2 Clean Cu(111) and Cu(211) surfaces

Cu is a noble metal with a face-centered cubic (fcc) structure and a lattice constant a=3.61 Å. The Cu(111) surface is close-packed with each atom surrounded by 6 neighbors in a hexagonal arrangement. A low resolution image of a typical Cu(111) surface revealing clean and flat terraces is shown in Figure 21a. A line profile across a part of the image shows a step edge with the step height of $\sqrt{3}/3a = 2.1$ Å as shown in figure 21b.

A high resolution STM image of the same surface reveals positions of individual atoms in the top-most atomic layer (Figure 24). The distances between neighboring atoms (nearest-neighbor distances) are $\sqrt{2}/2a = 2.55$ Å, the next-nearest-neighbor distances are $\sqrt{6}/2a = 4.4$ Å. Although we deal with a high purity and highly ordered Cu surface, surface and subsurface defects can regularly be observed. Point defects (e.g. substitutional and interstitial impurities, vacancies) disturb the crystal structure due to their sizes and different electronic structures.

Contrary to the Cu(111) surfaces the more corrugated vicinal Cu(211) surfaces show elongated atomic steps, with periodic ridges and groves along the $[0\bar{1}1]$ direction of the exposed surface layer (Figure 25). The top-most atoms form narrow (111)-facets separated by (100)-steps of monoatomic heights [67, 148]. The inter-row distances are 6.3 Å and the inter-atomic separation in the top-most atomic rows is 2.55 Å (Figure 26). The height of a single step is 0.74 Å. Individual Cu atoms are often displaced from their equilibrium positions in the uppermost Cu chains, as shown in the inset of Figure 25. These are probably a result of Ar^+ ion etching and insufficient annealing during the cleaning procedure.

Stepped (211) surfaces of fcc crystals are usually used to increase the control of the STM induced lateral manipulation of atoms and especially larger molecules, because of the strong anisotropy of the diffusion barrier (the diffusion barrier in the direction perpendicular to the intrinsic steps is expected to be much larger then in the parallel direction).

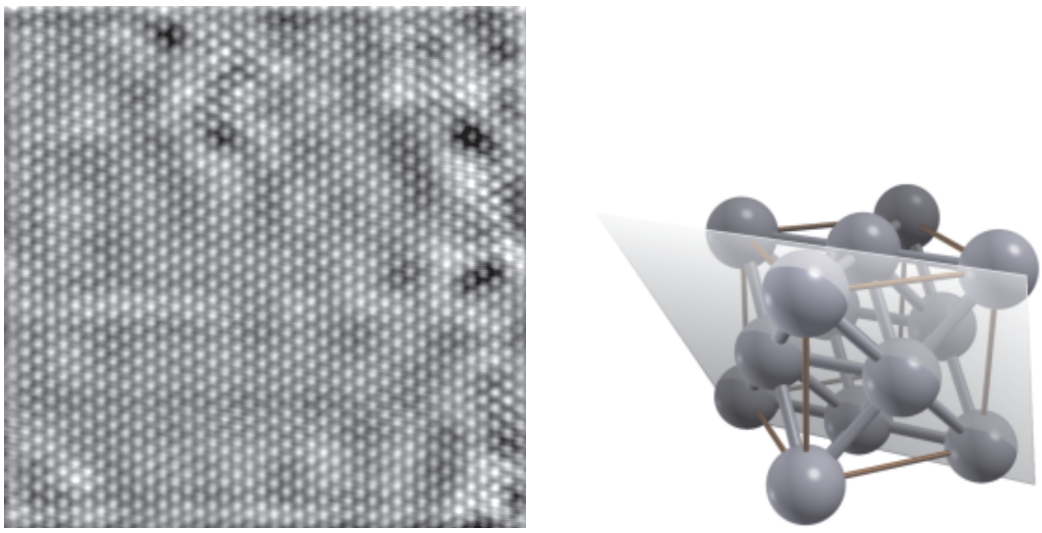

(a) (b)

Figure 24: a) Atomic resolution LT-STM image of a typical Cu(111) surface area. Subsurface defects perturb the crystal structure, which appears as a corrugation of the surface layer atoms. Area size $8 \times 8\,\mathrm{nm}^2$, $I_T = 2.2\,\mathrm{nA}$, $U_T = 190\,\mathrm{mV}$, $T = 9\,\mathrm{K}$. (b) The (111) plane in the Cu fcc lattice.

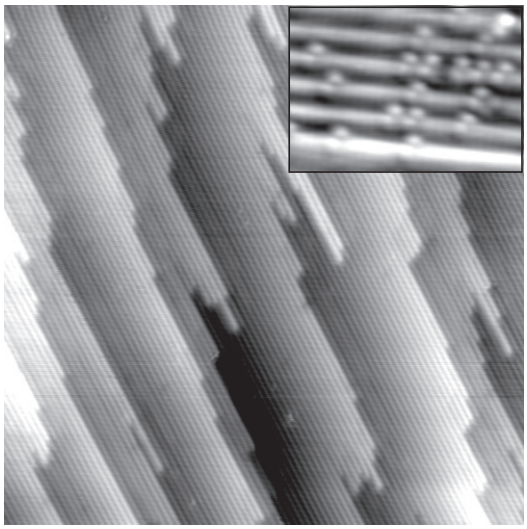

Figure 25: A LT-STM image of a Cu(211) surface with periodic ridges and groves along the $[0\bar{1}1]$ direction. Displaced Cu atoms in the uppermost Cu chains are probably a result of ion etching and are shown in the inset. Area size $55 \times 55\,\mathrm{nm}^2$, $I_T = 0.44\,\mathrm{nA}$, $U_T = 167\,\mathrm{mV}$, $T = 12\,\mathrm{K}$.

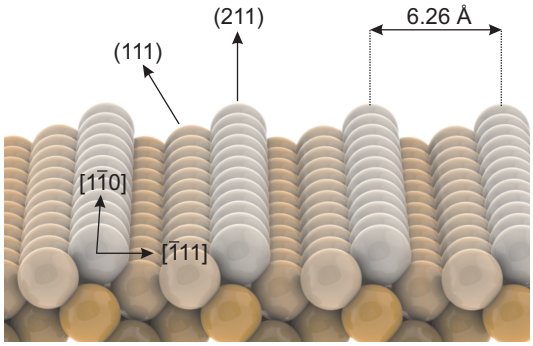

Figure 26: Hard-sphere model of the Cu(211) surface. The orientations of the micro facets and the crystal directions are indicated.

4.3 Surface-state electrons standing waves

If the electrons in a solid metal are restricted to a region close to the surface, their states are called Shockley surface states [168]. On close-packed nobel metal surfaces, the nearly free 2-D gas of electrons is highly isotropic [169] and scattered by step edges, dislocations, point defects and adsorbates. Such scattering perturbs the surface state charge density and leads to wave-like patterns, which can be directly imaged by the STM [26,170,171]. Recently induced charge density oscillations on the surface have been studied and used for mapping of the buried defects and interfaces [172].

An example is shown in Figure 27 where single adatoms act as the scattering centers for s-p derived Cu(111) surface state electrons. Standing waves with a wave vector $2k_F$ are clearly revealed. At the Fermi level E_F, surface state electrons have a wavelength of approximately 14 inter-atomic distances, but since the STM is sensitive to the square of the wavefunction $|\psi(r)|$ the wavelength of the wave vector appears half shorter. The wave vector k_F is extracted from the 2D Fourier-transform of the corresponding STM image (inset of Figure 27). A wavelength λ_F of 1.4 nm was measured for the surface state electrons at E_F, which is in good accord with the previously published data [173].

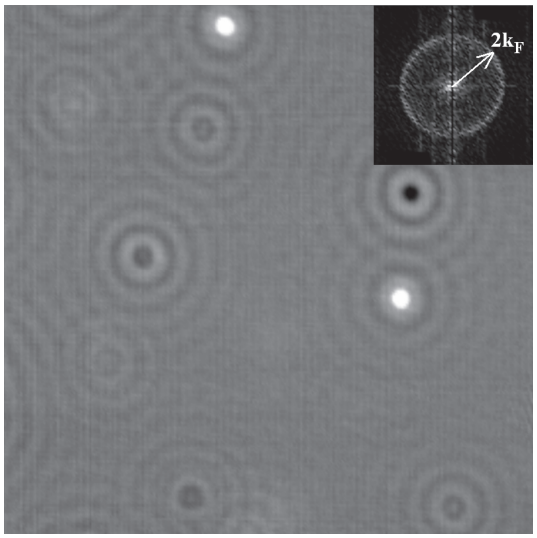

Figure 27: Constant current image of a Cu(111) surface with point defects and low amplitude standing electron waves with a vector $2k_F$. (inset) The power spectrum of the 2D Fourier transform provides a direct image of the Fermi contour. Area size $350 \times 350\,\mathrm{nm}^2$, $I_T = 1.11\,\mathrm{nA}$, $U_T = 105\,\mathrm{mV}$, $T = 8\,\mathrm{K}$.

4.4 Impurities on Cu(111) surfaces

When a clean sample was kept in UHV for an extensive period of time a surface contamination with carbon monoxide (CO) molecules (Figure 28) was observed. These were a result of the presence of residual gases[3] and were not deposited intentionally. CO is adsorbed on the top site on Cu(111) surface with carbon atoms down [147] and imaged by a clean metallic tips as depressions (dark spots) [92]. If a CO molecule is transferred onto the STM tip, the molecules in the images appear as protrusions (bright spots).

When imaged at elevated temperatures, the molecules were displaced under the effect of the STM tip, even at larger tip-sample separations. The worm-like linear structures (shown in Figure 29), that appear from top to bottom of the recorded images, are believed to be the CO molecules being pushed in front of the tip during successive line scans[4]. The displacement probability is a function of the tunneling current, the tunneling voltage and the temperature of the sample. Higher temperatures and reduced tip-sample distances lead to a greater probability of pushing the molecules across the surface.

[3] The residual gas inside the system consists essentially of He and small amounts of H_2, CO, H_2O, CH_3 and CH_4.

[4] The scanning is performed from top to bottom and from left to right and vice-versa.

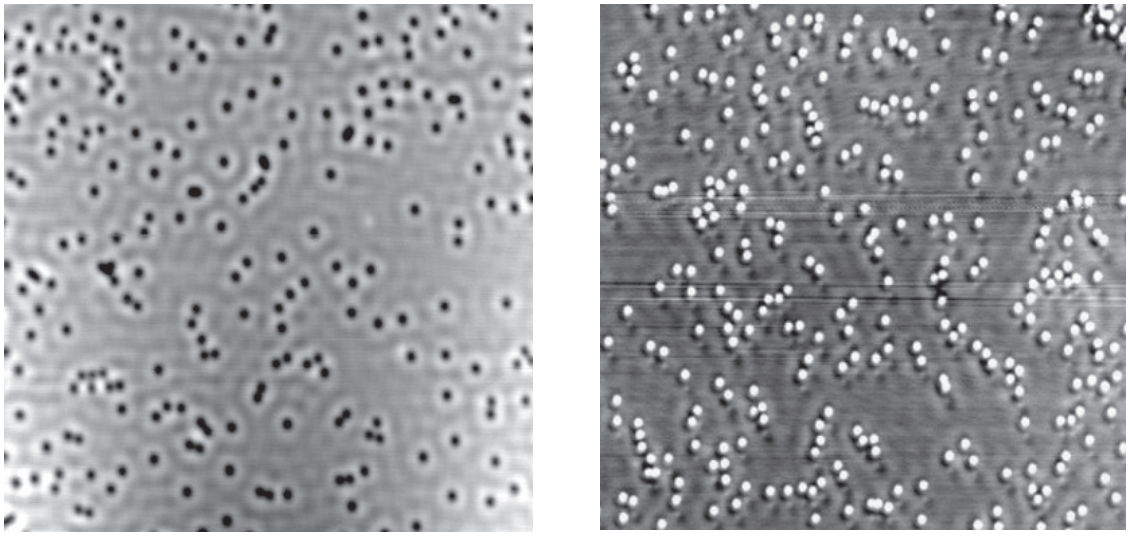

(a) (b)

Figure 28: LT-STM images of CO molecules on a Cu(111) surface. The molecules appear as depressions when imaged with a clean STM tip (a) or as protrusions if the tip is terminated by a CO molecule (b). Both: area size $150 \times 150\,\mathrm{nm}^2$, $I_T = 0.3\,\mathrm{nA}$, $U_T = 60\,\mathrm{mV}$, $T = 15\,\mathrm{K}$.

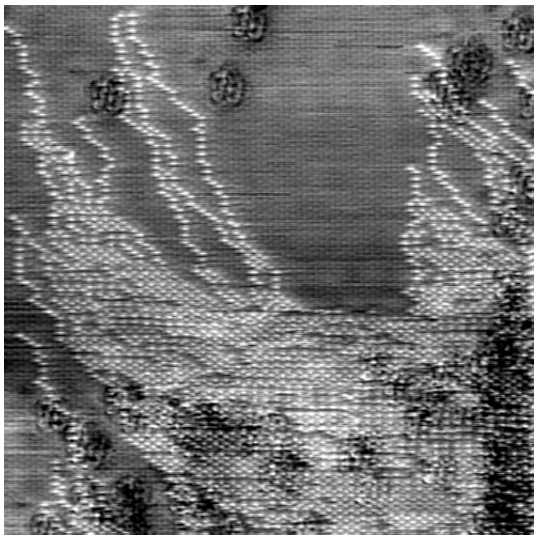

Figure 29: The CO molecules are pushed in front of the STM tip during scanning of a Cu(111) surfaces at higher temperatures. This produces worm-like linear structures on the recorded images. Area size $45 \times 45\,\mathrm{nm}^2$, $I_T = 1.84\,\mathrm{nA}$, $U_T = 64\,\mathrm{mV}$, $T = 23\,\mathrm{K}$.

Figure 30 shows a STM image of a nearby surface area after the tip was heavily crashed into the sample. The surface is covered with different adatoms and molecules. Although it is impossible to identify the individual species, they are still clearly distinguished by their apparent heights.

Another way of obtaining atomic resolution images of surfaces with very small electron lattice corrugations is to perform *manipulated atom imaging* [174]. The images are formed by scanning the tip over the surface using parameters that result in a small tip-sample separation[5] and with a trapped adatom in the tip-induced potential. An example is shown in Figure 31. The image was recorded with a Cu adatom trapped under the STM tip.

The probability of unintentional crashing and thus damaging the tip when working with the STM is in general low. However this can happen when samples are changed or if the UHV system is mechanically disturbed during operation. The quality of the tip usually degrades in case the impurities from the surface are transferred onto the tip or rarely, spontaneously, during work with higher tun-

[5]This is done by imaging with low values of $R = U_\mathrm{T}/I_\mathrm{T}$.

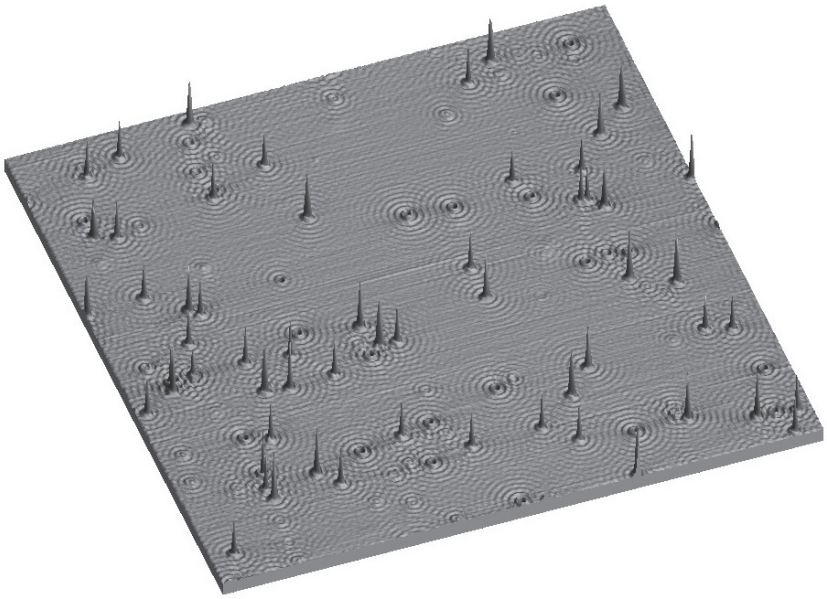

Figure 30: Large area LT-STM image showing different point defects, surrounded by standing electron waves. Area size $150 \times 150\,\mathrm{nm}^2$, $I_T = 0.81\,\mathrm{nA}$, $U_T = 51\,\mathrm{mV}$, $T = 7\,\mathrm{K}$.

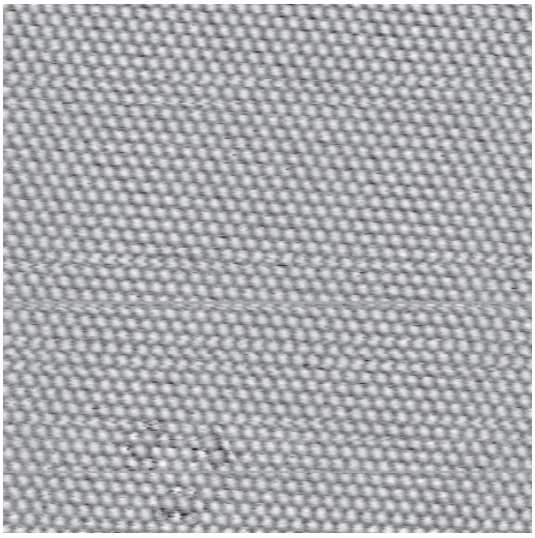

Figure 31: If an adatom is trapped in the tunneling junction a manipulated atom image is obtained, enabling atomic resolution on weakly corrugated Cu(111) surface. Area size $10 \times 10\,\mathrm{nm}^2$, $I_T = 83.0\,\mathrm{nA}$, $U_T = 30\,\mathrm{mV}$, $T = 7.5\,\mathrm{K}$.

neling voltages. An example of STM tip contamination is shown in Figure 32 where an impurity was transferred from a surface agglomerate onto the tip, which resulted in a *double-tip*. The recorded image appears as two overlapped identical images, displaced by the distance between the two apexes of the double-tip.

4.5 Adatom extraction and manipulation

As mentioned before, the STM tips can be in-situ reconditioned by a controlled tip-sample interaction [125]. The parameters which have to be varied are the speed and the depth of the indentation of the tip into the sample surface and the tunneling voltage. If the tip is crashed slowly into the sample surface by a few nm and at a low tunneling voltage, a clean, metal covered tip apex is obtained, which is usually very sharp[6]. Figure 33a shows an indentation produced during such a tip reconditioning

[6]While STM requires as sharp as possible tips, best STS measurements are performed with slightly blunt tips, which show less sharp peaks in tip DOS and ensure a better reproducibility of the spectra measured.

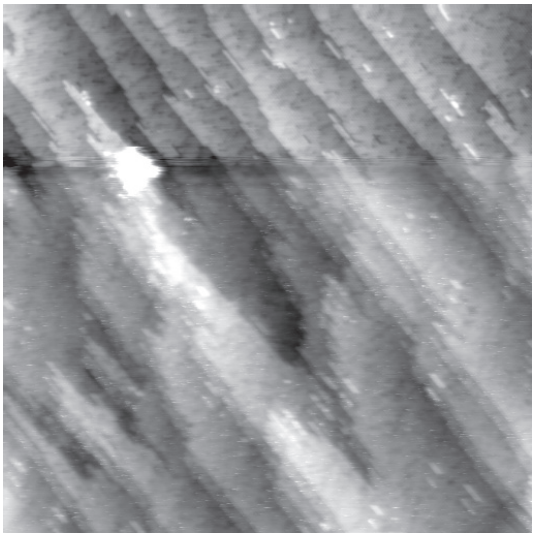

Figure 32: An adsorbate (probably a molecule) was transferred onto the STM tip during scanning over a large cluster of impurities. This resulted in a formation of a double tip. Area size $140 \times 140\,\mathrm{nm}^2$, $I_T = 0.56\,\mathrm{nA}$, $U_T = 405\,\mathrm{mV}$, $T = 15\,\mathrm{K}$.

procedure. Notice that there is almost no material found around the crash site. The substrate atoms were transferred onto the tip, which resulted in an elongation of the tip. If the applied tunneling voltage or the speed are increased, the procedure will result in an indentation with a large amounts of the substrate material piled up in the form of larger clusters, monolayer thick islands and individual Cu adatoms on the surface next to the indented area (Figure 33b). Single atoms can be distinguished from their agglomerates, as shown in the inset of Figure 33b. While individual Cu atoms are always the smallest round shaped species, doublets are unstable and appear slightly blurred due to their permanent rotation [175], while triplets are considerably larger.

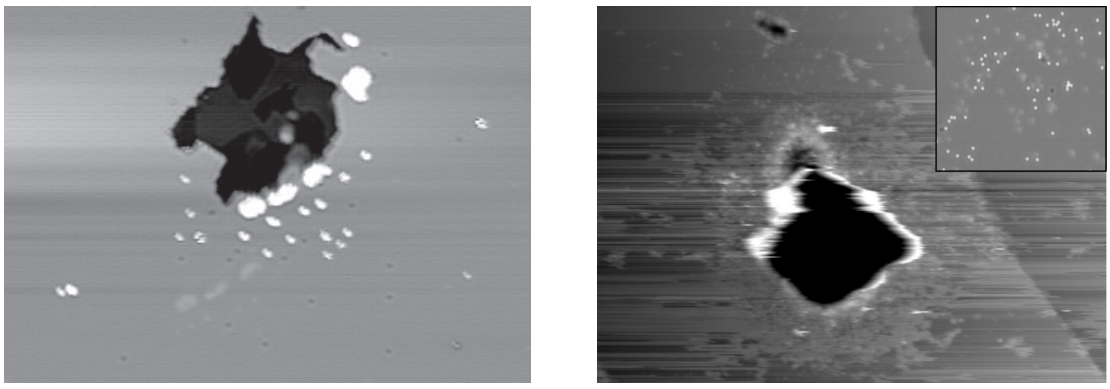

(a) (b)

Figure 33: A LT-STM image of a Cu(111) surface after a controlled tip-sample interaction with different parameters. (a) The material was transferred from the indentation area onto the tip which resulted in a metal coated and very sharp tip. (b) Atoms were ejected from the sample surface and individual Cu adatoms are visible in the inset, recorded close the indentation area. Area size (a) $50 \times 30\,\mathrm{nm}^2$, $I_T = 0.2\,\mathrm{nA}$, $U_T = 100\,\mathrm{mV}$, (b) $200 \times 120\,\mathrm{nm}^2$, $I_T = 0.35\,\mathrm{nA}$, $U_T = 40\,\mathrm{mV}$, both $T = 8\,\mathrm{K}$.

Individual Cu atoms produced in this way can be manipulated at low temperatures with the same STM tip by precisely controlling the quantum mechanical interactions. The constant-height mode lateral manipulation procedure involves exact positioning of the tip over the adatom, reduction of the distance between the tip and the adatom (resulting in stronger attractive forces), displacement of the tip (with the adatom) along a chosen path in a constant height mode, and finally retraction of the tip to the initial imaging height. Figure 34 shows a series of steps, needed for the construction a nanostructure, composed of 7 Cu adatoms.

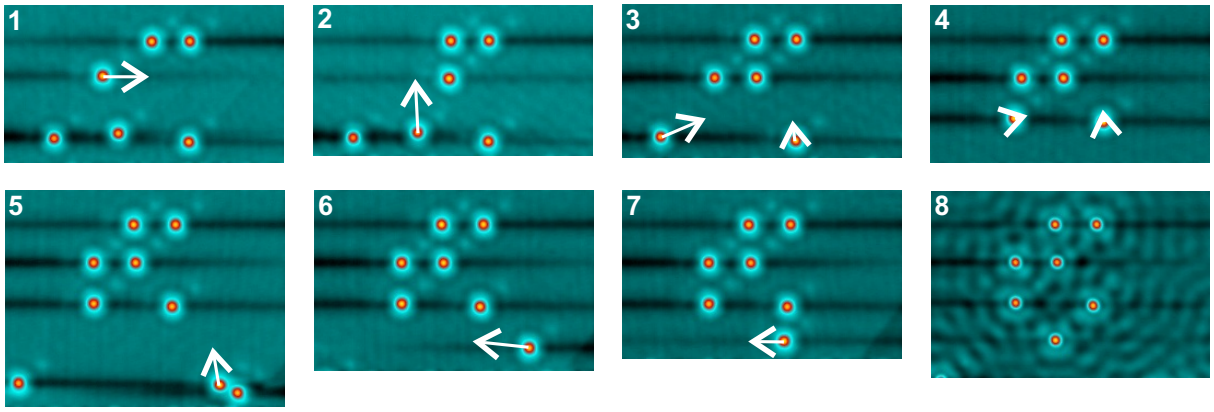

Figure 34: Individual steps of creating the Jozef Stefan Institute logo by means of a lateral push-mode manipulation procedure. The movements of the STM tip during Cu adatom displacements are shown in the images by white arrows. Images 1-7: width 18 nm, $I_T = 0.28$ nA, $U_T = 543$ mV. Image 8: width 18 nm, $I_T = 2.4$ nA, $U_T = 65$ mV. $T = 9$ K.

4.6 Scanning tunneling spectroscopy on Cu(111)

The STS measurements were performed on a clean Cu(111) surfaces as well as on individual Cu adatoms on these surfaces. It is clear from equation (2.3) that the tunneling current depends not only on the LDOS of the sample but also on the electronic structure of the STM tip. This is particularly important for the interpretation of the STS measurements. Figure 35 shows a differential conductance spectra recorded with different STM tips which all gave sharp, stable and symmetric images, but very different STS spectra. The geometry of these tips was obviously appropriate for STM imaging but the chemistry of the tip apex makes them unusable for STS experiments.

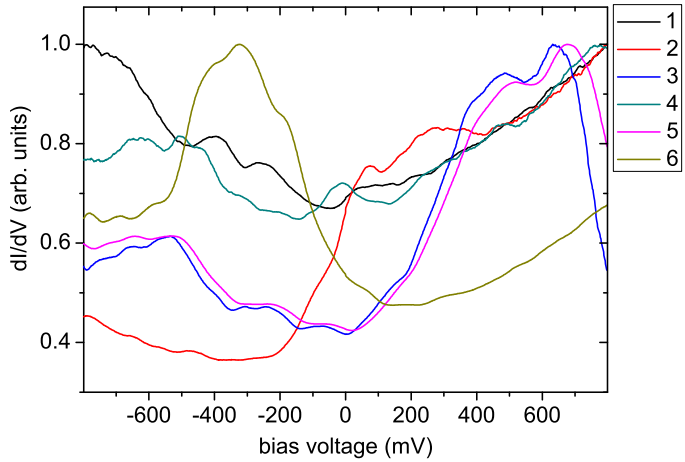

Figure 35: STS spectra, recorded over a clean Cu(111) surface with different STM tips, which all produced sharp and symmetric images. Since the measured spectra are always a combination of both, the tip and the sample DOS, clean and relatively blunt metallic tips are to be used for STS measurements. $V_m = 20$ mV.

Before measuring the electronic structure of the adsorbates the tip was reconditioned until the images of adatoms were spherical and the STS spectra recorded on the bare surface showed generic Cu(111) features with no spurious sharp features near zero bias. In Figure 36 two series of STS spectra recorded on the clean Cu(111) surface and on the isolated Cu adatom are shown. The spectra recorded on the clean and flat surface are in accord with the existing measurements and show a clear depletion in the LDOS at about 450 mV below the Fermi energy E_F, which is interpreted as the band edge of the Cu surface state [176]. It was shown that the width δ of the onset in Figure 36 is directly related to the lifetime of the holes at the surface state band-edge [177]. The measured width δ of 37 mV and the calculated lifetime τ of 22 fs are in good agreement with previous measurements [178]. The spectra recorded on the isolated Cu adatom exhibit a clear peak at 490 mV below E_F with a

full-width at half-maximum (FWHM) of 150 mV, which shows the presence of an adatom induced localization of the Shockley surface state [179]. In case the measurements are performed in a wider range, i.e. between -3V and +3V, more such depletions are clearly detected at different energies.

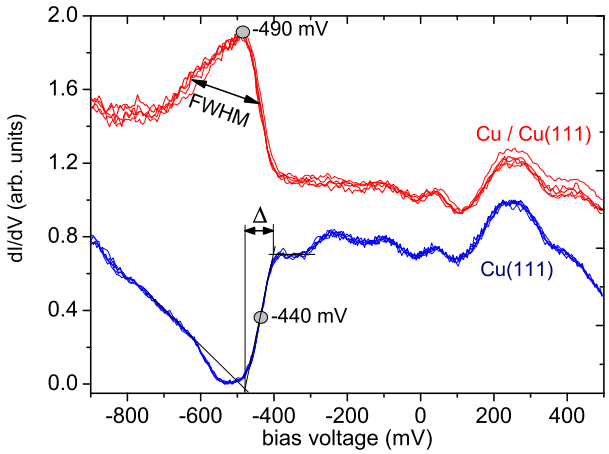

Figure 36: Two series of differential conductance spectra dI/dV, measured on a clean Cu(111) surface (blue) and on an isolated Cu(111) adatom (red). The width Δ of the onset is directly related to the lifetime of the electronic states. $V_m = 20\,\mathrm{mV}$.

It is obvious from Figure 36 that the dI/dV curves are fully reproducible. The quality of the recorded data depends largely on the amplitude of the modulating voltage and on the speed of the voltage sweep. Thus, high quality STS curves are obtained by optimizing the STS parameters and by averaging over a number of curves.

In addition to the spectra measured on the Cu(111) surface and on the individual Cu adatoms, STS was also performed along the 15 points marked in the inset of Figure 37. The characteristic resonance peak in the spectra vanishes rapidly in a continuous manner with the increasing distance from the Cu adatom, and the Cu surface state band edge slowly evolves. At about 2.5 nm from the adatom only the characteristic band edge is detected.

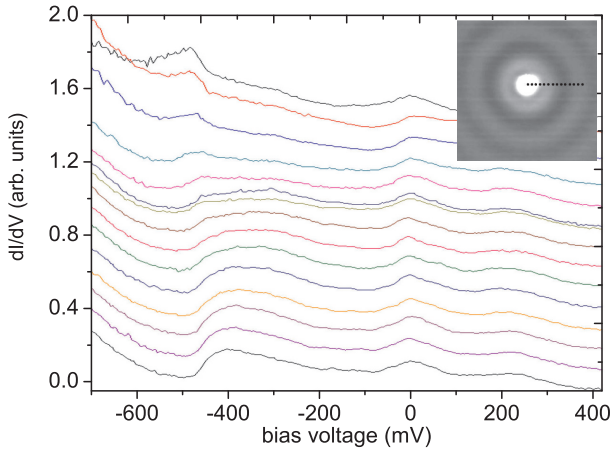

Figure 37: Differential conductance spectra dI/dV, measured on the 15 marked points, displaced by 0.2 nm. With increasing lateral tip displacement from the adatom the localization peak at -490 mV rapidly decays in intensity and the Cu surface state band edge at a sample bias of -440 mV evolves. The respective tip positions during STS measurements are marked in the inset. $V_m = 10\,\mathrm{mV}$.

4.7 Co nanoislands on Cu(111)

Evaporation of different metals or organic materials can be either carried out while the sample is kept at RT or in-situ with the sample cooled close to the LHe temperature. Co was evaporated onto a clean Cu(111) surface using a Knudsen source with the evaporation rate of $\sim$ 0.1 monolayers per

minute. Immediately after the deposition, the sample was quickly inserted into the precooled LT-STM in order to prevent intermixing of the deposited Co adatoms with the Cu atoms from the substrate, and segregation of Cu atoms onto the surfaces of the Co islands [180].

Deposition at RT resulted in a formation of Co islands [181–183]. When imaged, most Co islands were of triangular shape with a height of 2 monolayers above the surface (Figure 38a). Furthermore, one Co layer is believed to be buried into the Cu surface, forming three monolayers thick islands. The edges of the islands are aligned with the close-packed $< 1\bar{1}0 >$ directions of the Cu substrate. There are two possible island orientations, which correspond to the two sets of three-fold hollow sites on the Cu(111) surface. The existence of large islands indicates that Co atoms are highly mobile on a clean Cu(111) surface at RT, which is a common observation on the metal/metal systems. The STS spectroscopy measurements performed on the Co islands reveal the existence of a sharp peak, 310 mV below E_F, as shown in Figure 38b. The energetically localized state in the spectrum is believed to be due to the d-band electrons [184].

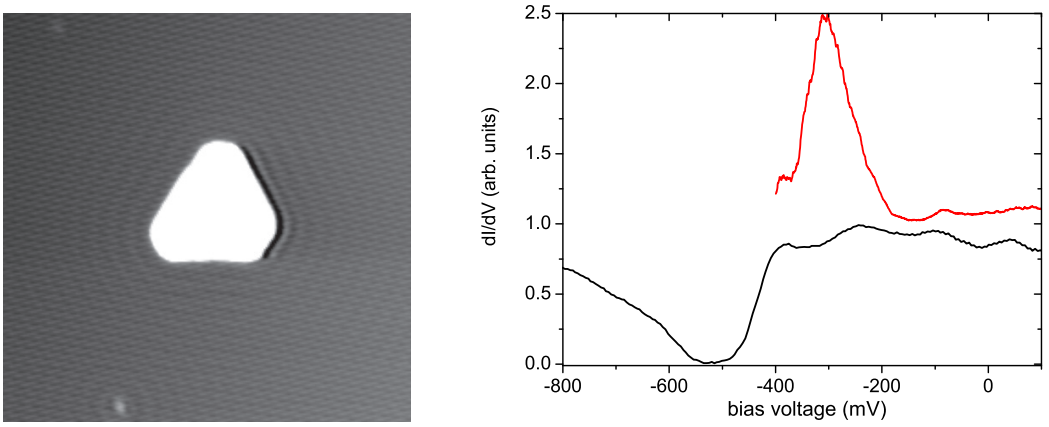

(a) (b)

Figure 38: (a)Triangular Co nanoisland, produced by RT deposition of Co from a Knudsen source. Area size $33 \times 33\,\mathrm{nm}^2$, $I_T = 0.4\,\mathrm{nA}$, $U_T = 166\,\mathrm{mV}$, $T = 12\,\mathrm{K}$. (b) STS spectra recorded on a clean Cu(111) surface (black) and on a Co island (red), showing a sharp peak at -310 mV bias voltage. $V_m = 10\,\mathrm{mV}$.

4.8 Summary

The stability and mobility of the surface adsorbates are strongly influenced not only by the temperature but also by the tip-sample interaction. While the tunneling currents used in STM and STS experiments are as low as 1 nA and below, they are spatially limited to areas of the order of single atoms, which results in huge current densities. The imaging resolution is also limited by thermal vibrations and mechanical drifts, caused by temperature gradients. To improve the spatial and energy resolution the experiments are to be performed at temperatures as low as possible.

Close to the LHe temperature the STM images of Cu(111) and Cu(211) surfaces clearly reveal, in addition to the periodic surface structures, a variety of adsorbates, impurities, point defects and related phenomena, like electronic standing waves. If the experiments are performed in an extremely clean environment and at sufficiently low temperatures, the mentioned structural imperfections are routinely detected. The wavelength λ_F of the surface state electrons at E_F was measured to be 1.4 nm.

The STS spectra, based on the dependence of the tunneling current on the gap voltage at a constant tip-surface separation, show an excellent reproducibility, which can be followed into the finest details of the spectra recorded. However, there is also a disadvantage, which makes these measurements tedious. These spectra depend on both, the shape and the chemistry of the particular tip used and the wave functions involved. Unfortunately, the actual shape of the tip is not known on an atomic scale. Thus, certain precautions are to be undertaken before unknown spectra are measured.

In the present case, the tip was repeatedly intruded into the Cu surface in a controlled way, until

the STS spectra measured on the Cu(111) surface verified characteristic features, such as the surface state band edge and no sharp peaks around zero bias. That was the only assurance that the apex of the tip was covered by Cu atoms and approximately round-shaped. Only with such tips measurements on single Cu adatoms were undertaken. The measured spectra show a characteristic small peak at about 40 mV below the deep edge at -450 mV, attributed to the Cu(111) surface states. This peak vanishes rapidly with increasing distance and is completely lost at about 2.5 nm from the center of the adatom. The surface-state lifetime in combination with the velocity determines the mean free path of the surface-state electrons and hence the effective excitation range. An advantage of measuring the lifetimes with STM is the ability to verify the local surface quality before performing the STM experiments and thus avoid effects from different defects. The lifetime τ for the holes at the surface state band-edge was measured to be 22 fs.

The described experiments represent a clear proof that STM and STS are two related methods, sufficiently accurate and sensitive to allow microscopic and spectroscopic measurements on an atomic scale. It is expected that characteristic spectra, measured on a variety of surface species, will gain importance in future nanotechnological processes and will enable identification of individual species, important for the local surface properties.

5 Embedded impurities in Cu(111) surfaces

Manipulation of single atoms by means of LT-STM represents an important step towards engineering of material properties in an atom-by-atom fashion. A detailed knowledge of the atomic-scale energetics and dynamics of elementary surface processes is not only of fundamental interest but also of major importance for the understanding of the stability, the properties and the behavior of such nanostructured materials. In spite of the enormous progress in this field, thermal stabilization of artificially assembled nanostructures remains a salient open problem.

In this chapter, a LT-STM study of stability of Co adatoms on Cu(111) surfaces as a function of temperature is presented. A detailed investigation of the properties of naturally occurring impurities embedded in the crystal surfaces and on their influence on the diffusion of Co adatoms was investigated. The relative position of pinned Co adatoms relative to the defects and the structure of pinned Co pairs were carefully examined by a combination of lateral manipulation and imaging procedures. The influence of embedded defects on the Kondo resonance of pinned Co adatoms was studied by detailed STS measurements. A series of calculations was performed in order to identify the defects. An additional experiment was conducted to verify the theoretical predictions.

5.1 Pinning of Co adatoms

A high-purity Cu(111) single crystal was prepared in UHV by the standard procedure of Ar^+ ion sputtering and annealing cycles. The sample was then transferred into the STM chamber and cooled to the working temperature. Submonolayer amounts of Co atoms were deposited from a high-purity (99.995 %) Co wire, wound around a resistive heated Mo filament (99.95 %). The wires were mounted outside the LN2 and LHe radiation shields and thoroughly degassed prior to the deposition[1]. The evaporation rate was controlled by the temperature of the Mo filament and thus by the temperature of the Co wire. The Co coverage was controlled by the opening times of the STM rotating radiation shields.

Topographic constant-current STM images of a clean and ordered Cu(111) surface show large flat terraces with a small amount of impurities, which are either adsorbed on the surface or embedded in the top-most and subsurface crystal layers. After in-situ deposition, isolated Co atoms appear in the images as $\sim$ 80 pm high bumps and they show characteristic standing waves in the form of concentric rings (Figure 39) [26]. When recorded at low enough temperatures, the Co adatoms remained at fixed positions. At higher temperatures most of them start to diffuse (free Co adatoms) while others, surprisingly, stay stable (pinned Co adatoms). The reason for their stability was studied into more detail by performing controlled atomic manipulations.

After the tip was lowered towards a pinned Co atom, the atom was displaced from its site by laterally repositioning the STM tip, as shown by the arrow in Figure 40a. With the adatom removed, the STM images revealed a faint feature at the position where the Co atom had been previously located, as indicated in Figure 40b. The apparent height of this feature is merely $\sim$ 8 pm. These defects could therefore easily remain undetected in the STM images of the bare Cu surface. In addition, no standing-wave pattern was visible around them. The defects had to be embedded in the surface, as an adsorbate on the surface typically exhibits not only large apparent height, but also produces significant standing-wave patterns. The conjecture of embedded substitutional impurity atoms is further supported by the fact that the defect cannot be displaced by the STM manipulation techniques. By carefully varying

[1]The UHV pressure during Co deposition never exceeded 2 x 10^{-10} mbar.

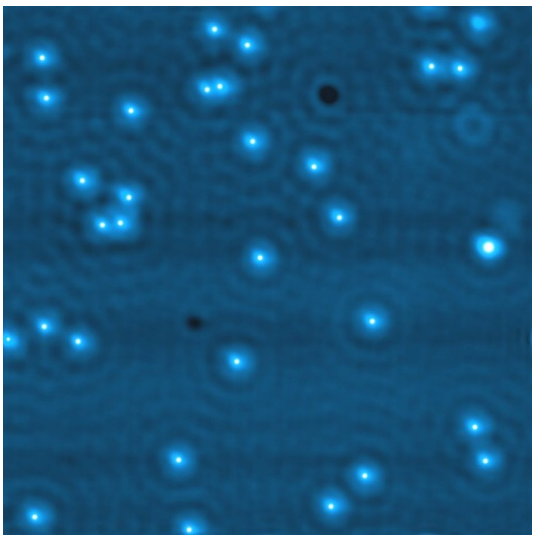

Figure 39: LT-STM image of a Cu(111) surface with individual Co adatoms. The adatoms were in-situ evaporated from a heated Co wire while the sample was at cryogenic temperatures. Area size $37.5 \times 37.5\,\mathrm{nm}^2$, $I_T = 0.95\,\mathrm{nA}$, $U_T = 80\,\mathrm{mV}$, $T = 8\,\mathrm{K}$.

different parameters of the sample preparation procedure, it was asserted that these impurities occur naturally and do not arise as sample contamination during preparation or sample transfer.

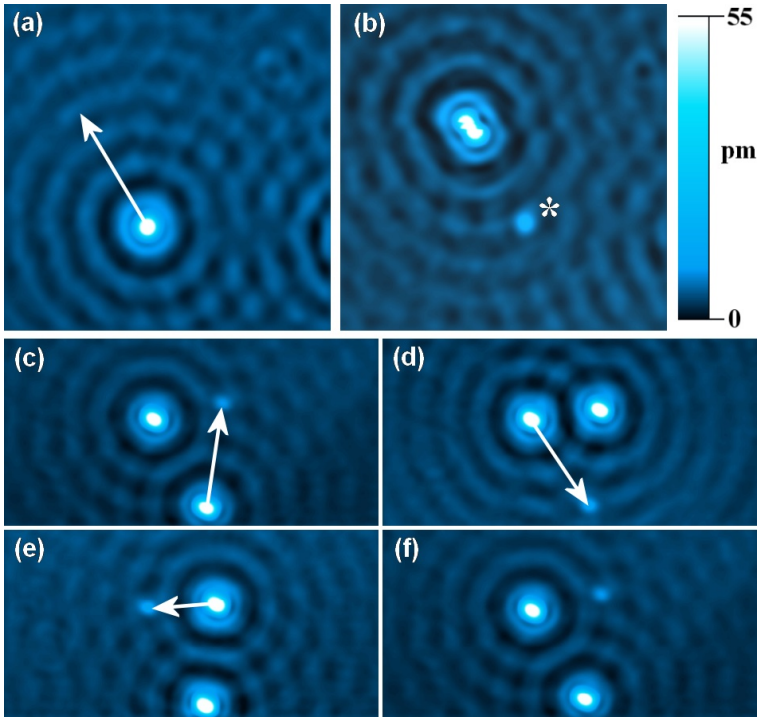

Figure 40: (a,b) Lateral manipulation of a Co adatom reveals an embedded defect (marked by *) at the pinning center. Above 8 K, the position of a depinned Co adatom is unstable and the atom appears blurred. The distance between the two discernible adsorbate positions in (b) is $0.26 \pm 0.04\,\mathrm{nm}$, which corresponds to the distance between two fcc binding sites. (c-f) The adatoms can be reversibly manipulated between three embedded defects. $I_T = 0.55\,\mathrm{nA}$, $U_T = 30\,\mathrm{mV}$, $T = 9\,\mathrm{K}$.

The Co adatoms can be displaced reversibly between different defect sites with the STM tip, as demonstrated in Figure 40c-f. The tunneling gap resistance needed to pull a Co adatom onto the defect site (or remove it from that position) is slightly lower than the one needed to manipulate it on a defect-free surface: the adatom has to overcome an additional potential barrier before it is pinned above an impurity. The Co adatoms, which had been displaced from the pinning sites are positionally unstable, show an apparent height reduced by about 4 pm, undergo random jumps

between neighboring adsorption sites and appear blurred as shown in Figure 40b. When the rest time of the Co adatom at a certain surface site is much longer then the image acquisition time (i.e., 20 s), the Co adatom appears as a sharp circular bump, surrounded by discernible concentric standing waves, Figure 40a. If, however, the rest time is comparable to the image recording time, the adatom appears as a combination of images with the adatom located at different surface sites, Figure 40b. The probability for such displacements increases with higher bias voltages.

Figure 41a presents a Cu(111) surface with different types of defects usually observed on this surface. The Co pinning sites are the two faint white defects, which are very different from the other defects. Their apparent height is only ~ 8 pm at a bias voltage of 100 mV (Figure 41b) and there is no standing-wave patterns around them (Figure 41a). Only at very high bias does the effective height increase (Figure 42), but still without concentric rings.

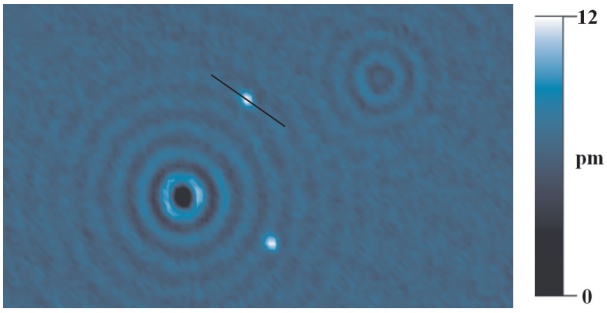

(a)

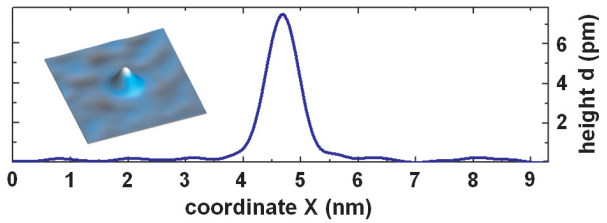

(b)

Figure 41: (a) Topographic LT-STM image ($35 \times 26\,\mathrm{nm}^2$) of typical defects on Cu(111) surface ($I_T = 1.0\,\mathrm{nA}$, $U_T = 100\,\mathrm{mV}$, $T = 7\,\mathrm{K}$). The embedded defects (white spots) show no standing-wave patterns. (b) The line profile across the embedded defect recorded at a gap voltage of $+100\,\mathrm{mV}$ (1 nA tunneling current) showing an apparent height of only $\sim 8\,\mathrm{pm}$.

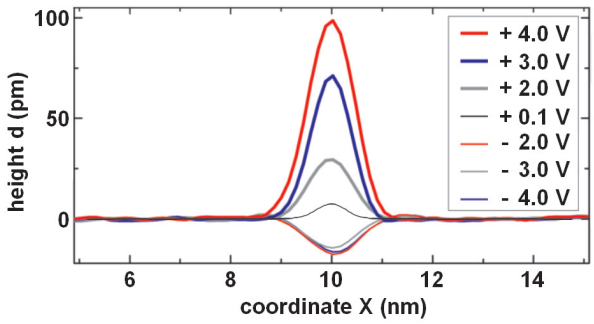

Figure 42: Topographic line profiles across the embedded defect in Cu(111) surface recorded for a range of bias voltages. $I_T = 1\,\mathrm{nA}$, $T = 7\,\mathrm{K}$.

The differences between the STS spectra recorded above a clean defect-free surface area and above the defects studied were found to be insignificant close to the Fermi level E_F and are increased with higher positive bias voltages (Figure 43). The embedded impurities were also studied with spatially-resolved STS mapping at different energies, which is a powerful and very discerning approach for studying electron scattering [63]. Figure 44 shows the result of a STS mapping of the selected surface. Figure 44a shows a constant-current image of the surface, recorded at $I_T = 1$ nA and $U_T = 100$

mV. Two embedded defects, showing no standing-wave patterns, and four other defects can clearly be resolved. Figure 44b shows changes in the tunneling current during image formation. Since the measurements were performed in the constant-current mode, the changes should be insignificant. Values of $dI/dV(U_T)$ are plotted as a function of tip position in Figure 44c. The modulation due to standing electron waves is now more pronounced but again, no standing waves are detected around the embedded defects. Figure 44d shows phase changes between the reference signal and the modulated tunneling current[2].

Similar measurements were carried out in the entire voltage range of stable STM operation with similar results. These strongly indicate that the scattering phase shift is very small in a rather wide energy interval around the Fermi level, which appears at a first glance highly unusual. It is however a clear indication of a chemical similarity between the host Cu atoms and the impurity atoms.

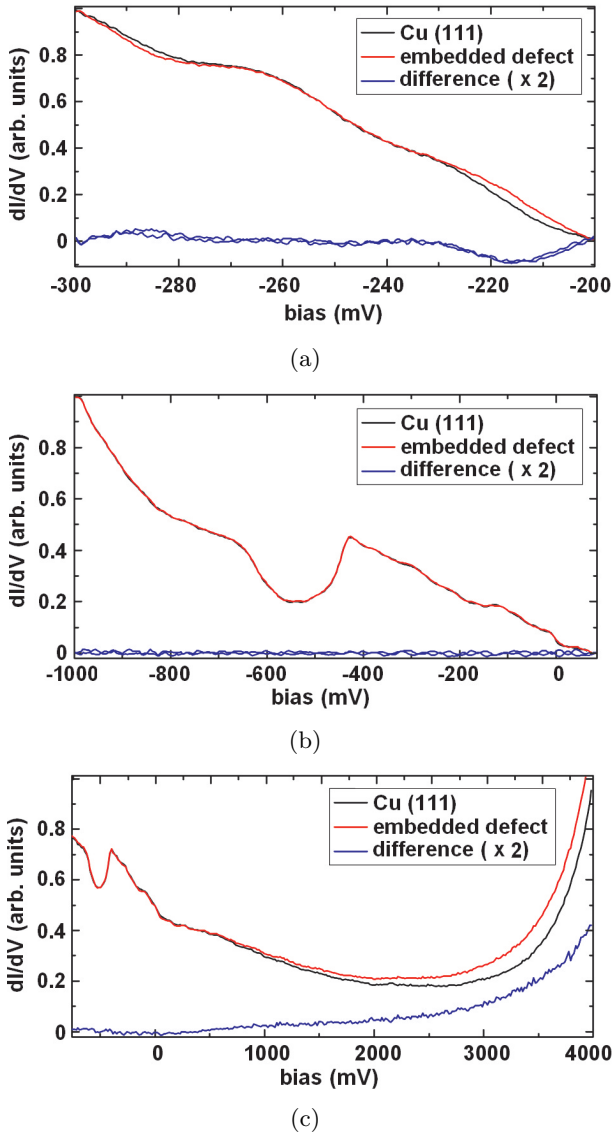

Figure 43: Scanning tunneling spectroscopy (STS) spectra measured over a clean and defect free Cu(111) surface (black curve) and over the embedded defect (red curve) for three energy ranges. The difference in differential conductivity is shown by the blue curve. The difference was found to be insignificant around the Fermi level E_F but increased with higher positive bias voltages. The embedded defect seems to induce a broad bound state just below the Cu band edge at $I = 4.2\,\mathrm{V}$ [185], thereby increasing the LDOS at higher biases. $V_m = 20\,\mathrm{mV}$.

We have also studied the effect of embedded defects on the magnetic coupling. The Kondo effect is characterized by a sharp zero-bias feature in the spectroscopy curves [72, 186–188]. The STS spectra were carefully measured around E_F in order to determine any effect of the embedded defects on the

[2]Lock-in amplifier measures the signal amplitude R which does not depend upon the phase difference.

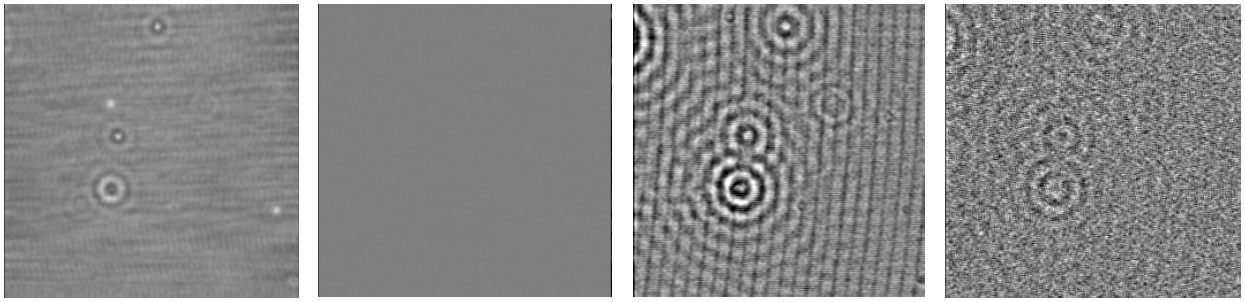

(a) (b) (c) (d)

Figure 44: STS mapping of the surface with two embedded defects. (a) A topographic constant-current image, (b) the tunneling current changes during scanning, (c) dI/dV value at eV_T and (d) phase changes of the signals. The electron standing wave patterns around embedded defects are still not detected, indicating the chemical similarity between the host Cu atoms and the impurity atom. Area size $38\times38\,\mathrm{nm}^2$, $I_T = 0.88\,\mathrm{nA}$, $U_T = 100\,\mathrm{mV}$, $T = 8.2\,\mathrm{K}$., $V_m = 10\,\mathrm{mV}$.

exchange coupling between the localized spin and the conduction-band electrons. The differences are, however, imperceptible: the Fano-resonance line-shape features in the tunneling spectra recorded with the STM tip over a trapped Co adatom show no significant differences as compared to those of a free Co adatom (Figure 45). This is surprising with regard to the high (exponential) dependence of the Kondo temperature on the atomic parameters.

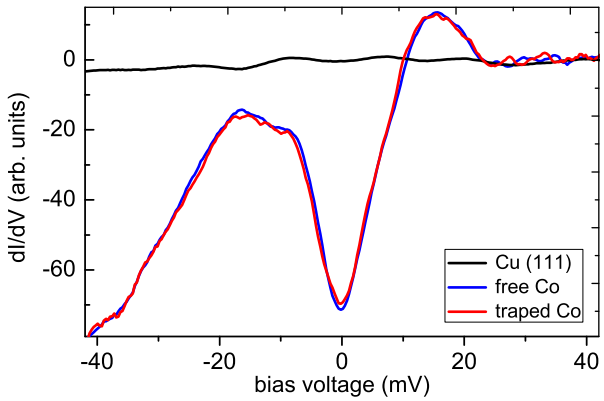

Figure 45: STS spectra at 7 K, measured by positioning the tip above a "free Co" adatom (blue curve) and above a "pinned Co" adatom (red curve). The Fano-like anomaly near the Fermi energy E_F is a characteristic feature of the Kondo effect, which occurs when conduction-band electrons from the substrate screen the local moment of the adsorbed Co atom. Tunneling parameters prior to opening the feed-back loop: $I = 1\,\mathrm{nA}$, $U = 100\,\mathrm{meV}$. $V_m = 2\,\mathrm{mV}$.

By laterally manipulating an adatom onto the defect position from different directions, all possible sites of the Co adatom relative to the defect were determined as shown in Figure 46a. The measured distances between the defect and the Co pinning sites of 0.26 ± 0.004 nm correspond to the distance between the substitutional defect and three fcc and three hcp interstitial sites on the Cu(111) surface (Figure 46b). These sites are not the nearest-neighbor interstitial sites, but rather the next-nearest-neighbor sites.

If the concentration of deposited Co atoms exceeds that of the embedded defects, STM images reveal the formation of Co pairs with adatoms separated by 0.56 ± 0.04 nm (Figure 47). This distance corresponds to that between the opposite fcc and hcp sites next to the defect. The pairs are stable and always oriented along one of the three equivalent $\langle 10\bar{1}\rangle$ directions. By removing the two adatoms, the embedded defect is revealed exactly halfway between them. Stable pairs at temperatures above 8 K can be constructed from free Co adatoms by manipulating them to the corresponding binding sites. Binding energy calculations show that there is some energy gain associated with the pair formation, but only about 13 meV.

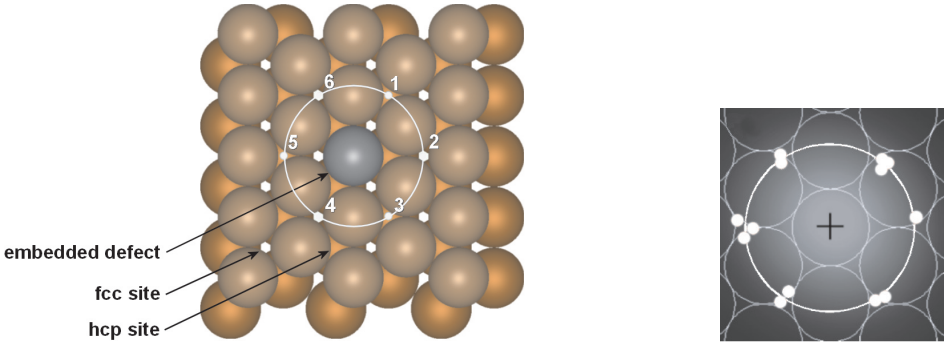

(a) (b)

Figure 46: (a) Top view of the model Cu(111) surface with an embedded defect. The Co adatom always occupies one of the six numbered fcc and hcp sites on the surface. (b) White dots are the experimentally determined binding sites of Co adatoms relative to the defect position.

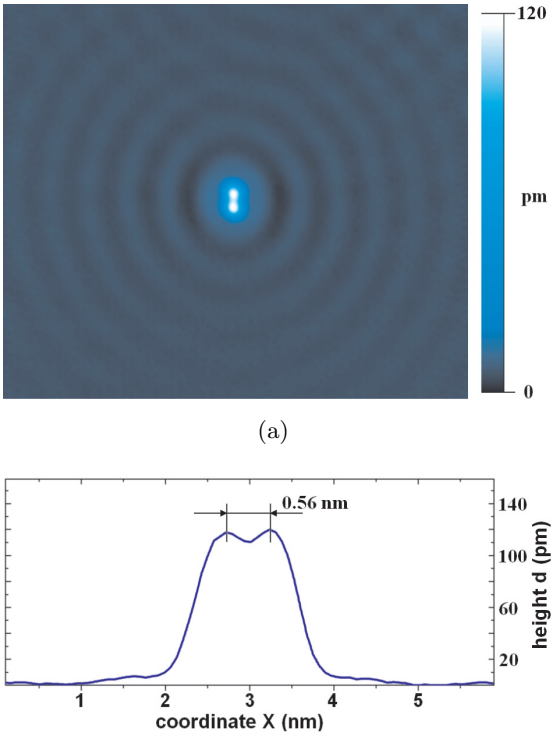

(a)

(b)

Figure 47: The structure of a pair of Co adatoms pinned to an embedded defect. The adatoms are separated by $0.56 \pm 0.04\,\mathrm{nm}$. Area size $19 \times 19\,\mathrm{nm}^2$, $I_T = 3.0\,\mathrm{nA}$, $U_T = 40\,\mathrm{mV}$, $T = 8\,\mathrm{K}$.

5.1.1 Introduction to Density Functional Theory

Density functional theory (DFT) is a most commonly used method to investigate ground state electronic structures of metals, semiconductors and insulators [189]. The method has the advantage of being versatile, it is able to treat problems with a sufficiently high accuracy and is computationally relatively simple (when compared to i.e. post-Hartree-Fock theory or quantum Monte Carlo, which are typically more precise). While DFT usually gives a good description of ground state properties, there are still difficulties when it is used for describing intermolecular interactions, strongly correlated systems and semiconductor band-gaps.

The main idea of DFT is to describe a system of fermions by its density rather than by its many body wave function. It is based on two Hohenberg-Kohn theorems [190]. These simplify the many body problem of N electrons with 3N spatial coordinates to 3 spatial coordinates through the use of functionals of the electron density. Using Kohn-Sahm equations [191], the unsolvable problem

of interacting electrons in a static external potential is reduced to the problem of a non-interacting electron in the effective potential produced by the remaining surrounding electrons; the problem then needs to be solved self-consistently. Finally, some approximations have to be included, since no exact functionals for the exchange and correlation effects are known. Usually two approximations are used in DFT, local-density approximation (LDA) and generalized gradient approximation (GGA).

In our calculations, performed by Rok Žitko, a plane-wave self-consistent field (PWSCF) code was used with a plane-wave basis set, ultrasoft pseudopotentials, and GGA exchange-correlation functionals [192–194]. This choice of parameters led to well-converged results, both for the local density of states at the Fermi level E_F and for structural relaxations (and binding energies).

5.1.2 Results of calculations

To compare the effect of different substitutional defects in the top-most layer of the Cu(111) surface on the electron structure in its vicinity, we have performed extensive computational studies. The LDOS at the Fermi level E_F was calculated in a plane 0.21 nm above the top-most layer of the surface Cu atoms. This distance roughly corresponds to the distance between the STM tip and the sample surface during scanning. The substrate surface was modeled using a three-layer slab geometry with the fcc (111) layers stacked perpendicular to the z-axis, while the width of the vacuum region was 1.25 nm. A 4-by-4 supercell was used along the x and y directions; such a relatively large size of the super-cell is required to correctly evaluate the lateral extent of the surface area where the LDOS is perceptibly perturbed by the defect. The lattice constant was optimized so that the energy of a clean Cu slab with fully relaxed inter-layer distances was minimized, yielding $a = 0.362$ nm. In subsequent calculations, the Cu atoms in the bottom-most layer were fixed, while all other atoms were still allowed to relax; at convergence, the smallest force was below 50 meV/nm. The geometry relaxation was found to be essential to obtain reliable adsorbate binding energies.

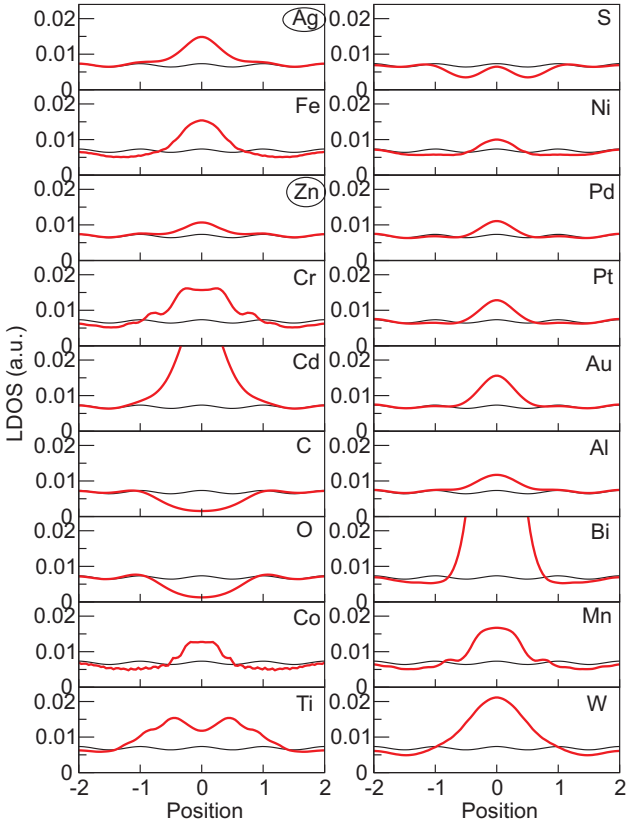

Figure 48: Comparison of calculated line profiles of the LDOS for a number of different impurities embedded in the top-most surface layer of the Cu(111) surface. The lines correspond to the $[1\bar{1}0]$ direction in the plane located 0.21 nm above the top-most layer of surface atoms. The horizontal axis corresponds to inter-atom distances along the $[1\bar{1}0]$ direction with the impurity atom located at the origin, i.e., at position 0. Only Ag and Zn are considered as likely candidates.

The calculations were performed for a large number of conceivable substitutional defects, including the known possible contaminants in the bulk crystal (Ag, Fe, Zn, Cr, Ca), the common surface contaminants on Cu (C, O, S), as well as other transition metal atoms in the neighborhood of Cu in the periodic system (Ni, Pd, Pt, Au) and some other elements. Figure 48 shows a comparison of calculated line profiles of the LDOS 0.21 nm above the top-most layer of atoms for different impurities, embedded in the Cu(111) surface. The impurity is located at the origin and the horizontal axis corresponds to the $[1\bar{1}0]$ direction. Among the likely impurities, only Ag and Zn substitutional atoms were found to induce a small change in LDOS which decays very rapidly with distance from the defect site. Pd, Pt, Au, and Al also exhibit a small change in LDOS, but are less commonly found as impurities in Cu single crystals in sufficiently high concentrations to be considered as plausible candidates. Other atoms yielded either a large change of the LDOS at the defect site (in some cases even of the opposite sign) or a perturbation with long-ranging tails, suggestive of a standing-wave pattern; neither of these cases agrees with the experimental results.

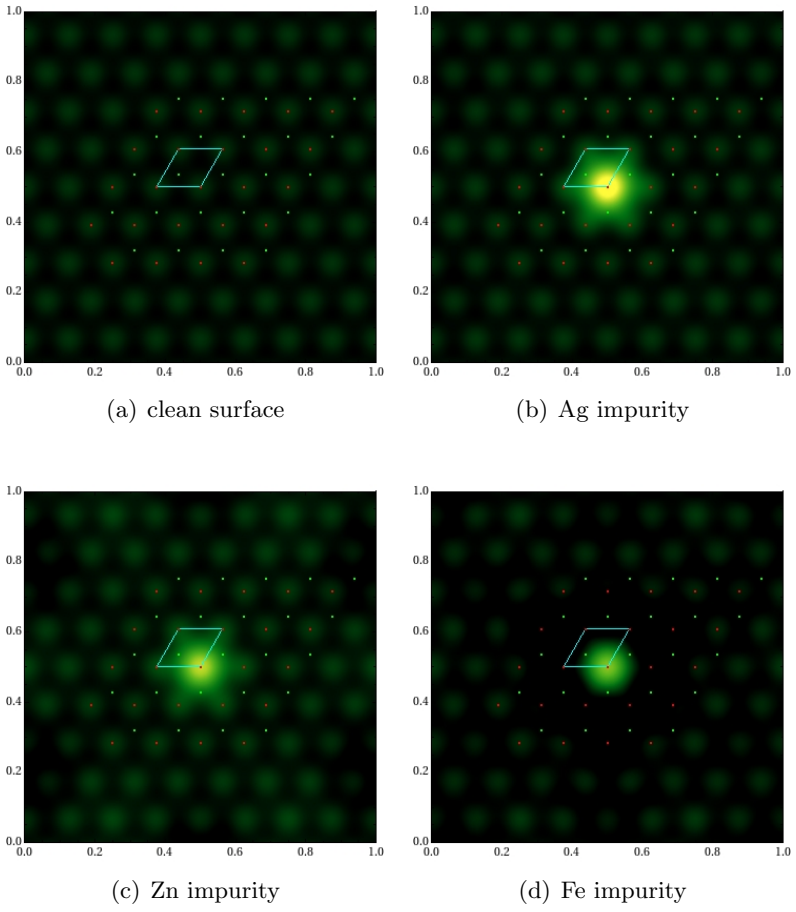

(a) clean surface (b) Ag impurity

(c) Zn impurity (d) Fe impurity

Figure 49: Calculated LDOS profiles along the plane 0.21 nm above the top-most layer of surface atoms. The cyan box indicates the lateral size of the unit cell, red dots correspond to the atomic positions in the top-most atomic layer, and green dots correspond to the atomic positions in the first subsurface (fcc)layer. Subfigure (d) demonstrates a dark ring of reduced LDOS surrounding a Fe impurity; no such features have been observed around the pinning centers, thereby Fe is not likely to be the embedded impurity.

In Figure 49 calculated profiles of LDOS are shown for a clean Cu(111) surface and for the two most plausible impurity candidates, Ag and Zn. Calculated LDOS for a Fe impurity is shown for comparison. These calculations have been performed using an 8-by-8 supercell in the transverse direction with the relaxed atomic positions taken from an initial DFT calculation performed in the 4-by-4 supercell.

Using the DFT, we have also studied the adsorption energetics. The calculated binding energy for a Co adatom on the clean surface is 3.222 eV for a fcc binding site, and 8 meV less for a hcp binding site, in agreement with previous studies [174]. The binding energy for a pinned Co adatom on a fcc binding site adjacent to an Ag defect is 3.315 eV, and 3.308 eV on a hcp binding site. Thus, the Co adatom effectively binds to the Ag defect with an additional energy of around 90 meV. The

binding energy for a Co adatom adjacent to a Zn defect is, however, only 2.3 eV, which means that the Co adatom is actually repelled from the hypothetical Zn defect. From these results, as well as from general theoretical considerations on the similarity of chemical properties of elements differing only in having additional completely-filled shells, it was concluded that the distinctive impurities can only be Ag atoms.

5.1.3 Experimental confirmation

To confirm this theoretical predictions we have performed a controlled deposition of Ag on a clean Cu(111) surface, followed by an annealing, performed with similar parameters as during the standard Cu surface cleaning procedure. Topographic images of such a surface showed a strongly increased concentration of pinning centers (Figure 50), which had the same topographic and spectroscopic characteristics as the native pinning centers.

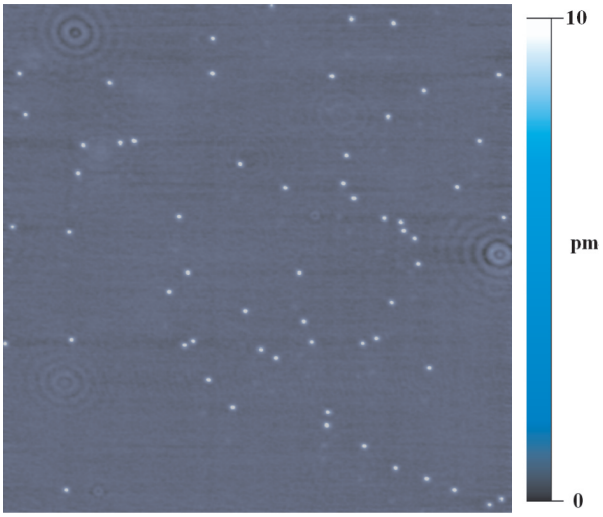

Figure 50: A topographic STM image of the Cu(111) surface ($75 \times 75\,\mathrm{nm}^2$) after a controlled deposition of small quantities of Ag atoms from a Knudsen source onto a clean sample surface and after annealing. $I_T = 1.0\,\mathrm{nA}$, $U_T = 100\,\mathrm{mV}$, $T = 7\,\mathrm{K}$.

5.2 Adatom diffusion

LT-STM is an excellent tool for studying individual atomic-scale processes of atoms and molecules on surfaces [30, 195–197]. The surface diffusion of a Co adatom, which is not pinned to any defect ("free" adatom) was monitored into more detail at different temperatures by tracking its position during a slow (10 mK per minute) temperature sweep from 8.2 to 9.5 K. The scanning was always performed with low bias voltages ($U_T < 10$ mV) to avoid STM tip induced motion of the adsorbates. Consecutive images were recorded at two-minute intervals and immobile surface defects provided markers for tracking the position of the mobile adatom. Its trajectory and the corresponding displacement lengths between consecutive scans are shown in Figure 51. At temperatures from 8.2 to $\sim$ 8.8 K, the adatom jumps between adjacent binding sites, which corresponds to a distance of 0.26 ± 0.04 nm [174]. At elevated temperatures, the enlarged diffusion rate results in longer displacements between consecutive images. In a similar temperature sweep for a pinned Co adatom, the adatom position was fixed up to 12.7 K; see red squares in Figure 51.

In case of a pinned Co adatom there is no telegraph noise present in the tunneling spectra when the tip is positioned above the adatom and the feedback is turned off, even at high bias voltages ($U_T < 100$ mV). We observed such a noise in case of free adatoms already at 7 K for bias voltages above 5 mV and it corresponded to a random hopping between the preferred fcc binding sites and the nearest-neighbor hcp sites due to inelastic electron tunneling [174]. Figure 52 shows voltage dependent adatom hopping, detected by abrupt jumps in the tunneling current. For pinned adatoms such processes are suppressed due to the additional binding by the embedded impurity.

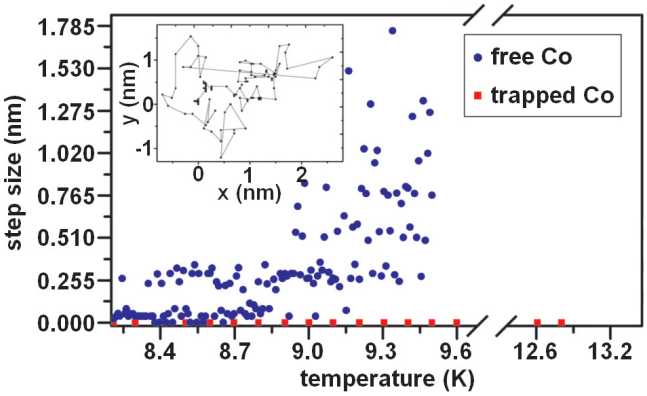

Figure 51: Surface diffusion of a "free" Co adatom on Cu(111) (blue filled circles) and the stability of a pinned Co adatom (red squares) at different temperatures. The step size is the distance between the positions of the particle in two consecutive images. The time interval between two images (data points) is 120 seconds. Note the discrete values of the displacements. The inset shows the recorded trajectory of the Co adatom during surface diffusion. The random motion of the Co adatom is not influenced by the STM tip, as the scanning direction is always from left to right and from top to bottom, whereas the displacements show no systematic drift. $I_T = 0.88\,\mathrm{nA}$, $U_T = 10\,\mathrm{mV}$.

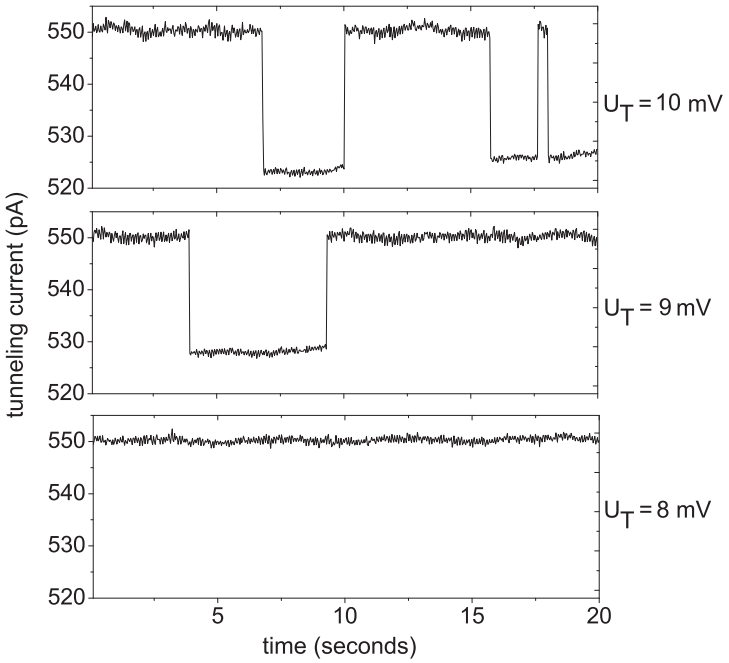

Figure 52: A telegraph noise is observed in the tunneling current if the tip is positioned above a Co adatom at constant height. The adatom hopping rate between neighboring binding sites is voltage and temperature dependent. $I_T = 0.51\,\mathrm{nA}$, $T = 7.3\,\mathrm{K}$.

5.3 Summary

A LT-STM was used to study the surface stability of Co adatoms on the Cu(111) surface. We have found that some of the adatoms are surprisingly stable: whereas most of the Co adatoms start diffusing already above 8 K, a small number of Co adatoms remain pinned up to 12.7 K.

Performing the lateral manipulation experiments it was found that these adatoms are positionally stabilized by impurity atoms, which are embedded in the underlying Cu(111) surface. These atoms show no standing-wave patterns and are hardly observable in the topographic images. By varying the parameters of the sample cleaning procedure we confirmed that the defects occurred naturally. Although the deposition of adatoms was performed at low temperatures, the increase in sample temperature during evaporation enables Co adatoms to diffuse on the sample surface and thus get pinned by the embedded defects.

By measuring the STS spectra we concluded that the defects did not affect the exchange coupling of the Co adsorbate with the substrate electrons. Thus the Kondo resonances measured on pinned and free Co adatoms show no detectable differences. We were also not able to detect any significant differences between STS measurements on the clean Cu(111) surface and those on the embedded impurity in a wide energy interval.

Using numerous DFT calculations to model the LDOS in the plane above different impurities and comparing them to the experimental data, the defects were identified as embedded Ag impurities. This prediction was further confirmed by an Ag deposition and annealing experiment.

The Co adatoms can be reversibly manipulated between embedded defects and even pairs of Co adatoms can be formed above an embedded Ag atom.

Our observation of the enhanced stability of Co adatoms on Ag impurities suggests the exciting possibility of using embedded defects as templates for building artificial atomic structures, which would remain stable at elevated temperatures. Furthermore, our results indicate that ordered surface alloys might support self-assembly of magnetic impurity lattices.

6 Conclusions

The scanning tunneling microscope (STM) is a modern and very versatile nanotechnological tool. It enables real space (and real time) atomic resolution imaging, single atom and molecule manipulation (lateral or vertical displacement of adsorbates, braking and forming chemical bonds, changing molecular conformation...). By measuring the local electronic structure (i.e. electronic density of states (DOS)) it is possible to investigate physical and chemical properties at an atomic level.

An existing ultra-high vacuum (UHV) system was upgraded with a liquid-helium (LHe) bath cryostat. Additional UHV chambers with a sample transfer mechanism were constructed. To reach UHV conditions, the entire system had to be baked to 110 °C.

A LHe cooled low-temperature (LT) STM operational at 7 K was constructed. Its high mechanical stability allows atomic resolution imaging of close-packed nobel metal surfaces such as Cu(111). Scanning tunneling spectroscopy (STS) measurements on Cu and Co adatoms and clean Cu(111) surfaces show a high energy resolution, limited by the finite temperature of the STM junction. The microscope is housed behind LHe and LN2 rotating radiation shields, being hanged on three stainless-steel springs and is damped by eddy currents. The LT-STM head is compatible with the Omicron sample holders in order to retain compatibility with the existing room-temperature (RT) STM.

The tips for STM microscopy were prepared by electrochemically etched W wires in a KOH solution with a home-made electronic circuit and afterwards cleaned in the hydrofluoric acid to remove W oxides. The tips were in-situ routinely reconditioned by a controlled tip-sample interaction. This resulted in metal covered, stable and sharp STM probes.

The cleaning of the Cu(111) and Cu(211) surfaces was performed by repeated Ar^+ ion sputtering and annealing cycles. The process was automated with a computer control. The surface quality was monitored by low-energy electron diffraction (LEED) and Auger electron spectroscopy (AES). The deposition of small amounts of materials was performed at room-temperature (RT) and at LT from a Knudsen evaporation source and by resistive heating of a Mo wire with the evaporation material wrapped around it, respectively.

Single crystal Cu(111) surfaces were recorded at the LHe temperature and under UHV conditions. They were characterized by clean and flat terraces and monoatomic steps. If recorded at higher magnifications individual atom were routinely revealed. Single impurities, adsorbed CO molecules and larger impurity clusters were typically found on these surfaces. Electronic standing waves of surface state electrons around surface and subsurface defects and next to step edges were regularly detected. Using Fourier-transform of the STM images, the wavelength λ_F of the surface state electrons at E_F was found to be 1.4 nm.

Cu(211) single crystal surfaces reveal irregular atomic steps, elongated along the periodic surface ridges and groves and often reveal single Cu atoms, displaced from their equilibrium positions in the uppermost Cu chains.

The STS, performed on a clean and flat Cu(111) surface, reveals a large depletion in the LDOS at 450 mV below E_F, which is attributed, in accord with literature, to the edge of the electronic surface state band structure. The lifetime τ of the holes at the surface state band-edge was measured to be 22 fs. STS of single Cu adatoms reveals a characteristic peak in LDOS some 50 mV below the edge of the surface electronic states with a full-width at half-maximum (FWHM) of 150 mV, attributed to a localization of the Cu(111) surface state. The peak vanishes rapidly with the distance from the adatom.

STS measurements require extreme STM stability and the results depend strongly on the STM tip geometry and chemistry. Performing spectroscopy with a clean, that is a metallic tip is thus essential

to get meaningful information on the local electronic structure. We noticed that for STS it is better to use slightly blunt tips, which don't show sharp peaks around the Fermi level E_F. When these criteria are met, STS curves show an excellent reproducibility.

Single Cu adatoms were extracted from the sample surface by intentionally crashing the STM tip. They were used to assemble different nanostructures with both push- and pull-mode lateral manipulation techniques. By trapping a Cu adatom under the STM tip, manipulated atom images of the Cu(111) surfaces showing atomic resolution were recorded.

Co nanoislands were grown on Cu(111) surfaces at RT using a Knudsen source. The deposition resulted in two-monolayer thick, triangular shaped islands, characterized by a peak in the corresponding STS curves, positioned 310 mV below E_F.

The deposition of Co onto a sample cooled to 7 K, resulted in isolated and stable Co adatoms. At elevated temperatures some of them started to diffuse across the sample surface, while others stayed stable. The reason for their stability are the underlaying substitutional surface defects in the Cu substrate surface. These defects show very low apparent heights of only ~ 8 pm and are characterized by an absence of the standing wave patterns around them.

Using density functional theory (DFT) calculations, LDOS at the Fermi level E_F above the impurities were simulated and compared with the experimental data. Additionally, binding energy calculations have been performed for the most probable candidates. From these calculations and by taking into account the similarity in chemical properties of the elements, which differ only in completely-filled shells, we concluded that the only probable impurity element was Ag.

The prediction was confirmed by an experiment, where small amounts of Ag atoms were deposited onto a clean Cu(111) surface and subsequently annealed. STM images of such surfaces show a strong increase in the concentration of embedded defects, which had the same topographic and spectroscopic properties as the previously studied ones.

The temperature dependent diffusion of free and trapped Co adatoms on the Cu(111) surface was also studied. It was found that the free adatoms start to diffuse already at temperature above 8.2 K, while the trapped adatoms stay stable up to 12.7 K.

The exact positions of Co adatoms relative to the embedded defects were determined by laterally manipulating the adatoms onto and from the defects. The Co adatoms were found to occupy one of the six next-nearest-neighbor sites. If the number of Co adatoms is increased, Co pairs are formed, which occupy opposite fcc and hcp sites next to the Ag defect.

7 Acknowledgements

I would like to sincerely thank my supervisor, prof. dr. Albert Prodan for teaching me how good experimental physics is done. Without his profound knowledge on the microscopy and the surface science this work would not be possible. Thanks to ass. prof. Miha Škarabot for being co-supervisor, for all the guidance and the advice during my work. I am very grateful to prof. dr. Igor Muševič for giving me the opportunity of working at the department and for being patient during the hard times. Many thanks to Rok Žitko for all his help during the numerous hours spend on building and operating the STM and for sharing his knowledge and views on science and everyday life. I acknowledge the valuable help of Stefan Fölsch from PDI on the experimental work and Ivan Kvasič for all the help on the electronic components.

Finally, I thank my parents for their lifelong support and Katja and Maks for all the love and for understanding and supporting my devotion to science. To them I dedicate this thesis.

References

[1] Feynman, R. P. There's Plenty of Room at the Bottom. http://www.its.caltech.edu/~feynman/plenty.html (accessed August 2010).

[2] Wiesendanger, R. *Scanning Probe Microscopy and Spectroscopy: Methods and Applications.* Cambridge University Press, (1994).

[3] Binnig, G., Rohrer, H., Gerber, C., and Weibel, E. *Phys. Rev. Lett.* **49**(1), 57–61 (1982).

[4] Binnig, G., Quate, C. F., and Gerber, C. *Phys. Rev. Lett.* **56**(9), 930–933 (1986).

[5] Pohl D. W., D. W. and M., L. *Appl. Phys. Lett.* **44**, 651 (1984).

[6] Binnig, G., Rohrer, H., Gerber, C., and Weibel, E. *Appl. Phys. Lett.* **40**, 178 (1982).

[7] Binnig, G., Rohrer, H., Gerber, C., and Weibel, E. *Phys. Rev. Lett.* **50**(2), 120–123 (1983).

[8] Foster, J. S. and Frommer, J. E. *Nature* **331**, 324 (1988).

[9] Becker, R. S., Golovchenko, J. A., and Swartzentruber, B. S. *Nature* **325**, 419 (1987).

[10] Eigler, D. and Schweizer, E. K. S. *Nature* **344**, 524 (1990).

[11] Hla, S.-W., Bartels, L., Meyer, G., and Rieder, K.-H. *Phys. Rev. Lett.* **85**(13), 2777–2780 (2000).

[12] Liljeroth, P., Swart, I., Paavilainen, S., Repp, J., and Meyer, G. *Nano Letters* **10**(7), 2475–2479 (2010).

[13] Repp, J., Meyer, G., Stojković, S. M., Gourdon, A., and Joachim, C. *Phys. Rev. Lett.* **94**(2), 026803 (2005).

[14] Qiu, X. H., Nazin, G. V., and Ho, W. *Science* **299**(5606), 542–546 (2003).

[15] Wiesendanger, R., Güntherodt, H.-J., Güntherodt, G., Gambino, R. J., and Ruf, R. *Phys. Rev. Lett.* **65**(2), 247–250 (1990).

[16] Serrate, D., Ferriani, P., Yoshida, Y., Hla, S.-W., Menzel, M., von Bergmann, K., Heinze, S., Kubetzka, A., and Wiesendanger, R. *Nature Nanotechnology* **5**, 350–353 (2010).

[17] Leonard C. Feldman, J. W. M. *Fundamentals of Surface and Thin Films Analysis.* North-Holland, (1986).

[18] Chen, C. J. *Introduction to Scanning Tunneling Microscopy (Monographs on the Physics and Chemistry of Materials), 2 edition.* Oxford University Press, USA, (2007).

[19] Hans-Joachim Guntherodt, Roland Wiesendanger, D. A. R. B. P. v. B. S. C. R. H. H. v. K. Y. K. H. R. J. W. *Scanning Tunneling Microscopy I: General Principles and Applications to Clean and Adsorbate-Covered Surfaces (Springer Series in Surface Sciences).* Springer, (1992).

[20] H-.J. Guntherodt, R. W., editor. *Scanning Tunneling Microscopy II: Further Applications and Related Scanning Techniques (Springer Series in Surface Sciences).* Springer-Verlag Berlin and Heidelberg GmbH & Co. K, (1995).

[21] Bonnell, D., editor. *Scanning Tunnelling Microscopy and Spectroscopy: Theory, Techniques and Applications*. Wiley-Blackwell, (2001).

[22] Drakova, D. *Reports on Progress in Physics* **64**(2), 205 (2001).

[23] Hofer, W. A., Foster, A. S., and Shluger, A. L. *Rev. Mod. Phys.* **75**(4), 1287–1331 (2003).

[24] Hofer, W. A. *Progress in Surface Science* **71**(5-8), 147 – 183 (2003). Proceedings of the IXth Symposium on Surface Physics, Trest Castle 2002.

[25] Briggs, G. A. D. and Fisher, A. J. *Surface Science Reports* **33**, 3 (1999).

[26] Crommie, M. F. *Journal of Electron Spectroscopy and Related Phenomena* **109**(1-2), 1 – 17 (2000).

[27] Fiete, G. A. and Heller, E. J. *Rev. Mod. Phys.* **75**(3), 933–948 (2003).

[28] Besenbacher, F. *Reports on Progress in Physics* **59**(12), 1737 (1996).

[29] Wiesendanger, R. *Rev. Mod. Phys.* **81**(4), 1495–1550 (2009).

[30] van Houselt, A. and Zandvliet, H. J. W. *Rev. Mod. Phys.* **82**(2), 1593–1605 (2010).

[31] Fischer, O., Kugler, M., Maggio-Aprile, I., Berthod, C., and Renner, C. *Rev. Mod. Phys.* **79**(1), 353–419 (2007).

[32] Meyer, G., Repp, J., Zöphel, S., Braun, K.-F., Wai-Hla, S., Fölsch, S., Bartels, L., Moresco, F., and Rieder, K.-H. *Single Molecules* **1**, 79 (2000).

[33] Komeda, T. *Progress in Surface Science* **78**(2), 41 – 85 (2005).

[34] Moresco, F. *Physics Reports* **399**(4), 175 – 225 (2004).

[35] Hla, S.-W. *Journal of Vacuum Science & Technology B: Microelectronics and Nanometer Structures* **23**(4), 1351–1360 (2005).

[36] Ho, W. *J. Chem. Phys.* **117**, 11033 (2002).

[37] Lorente, N., Rurali, R., and Tang, H. *Journal of Physics: Condensed Matter* **17**(13), S1049 (2005).

[38] Grill, L. *Journal of Physics: Condensed Matter* **22**(8), 084023 (2010).

[39] Giaever, I. *Phys. Rev. Lett.* **5**(4), 147–148 (1960).

[40] Lang, N. D. *Phys. Rev. B* **34**(8), 5947–5950 (1986).

[41] Bardeen, J. *Phys. Rev. Lett.* **6**(2), 57–59 (1961).

[42] Tersoff, J. and Hamann, D. R. *Phys. Rev. Lett.* **50**(25), 1998–2001 (1983).

[43] Tersoff, J. and Hamann, D. R. *Phys. Rev. B* **31**(2), 805–813 (1985).

[44] Feenstra, R. M., Stroscio, J. A., Tersoff, J., and Fein, A. P. *Phys. Rev. Lett.* **58**(12), 1192–1195 (1987).

[45] Rost, M. J., Crama, L., Schakel, P., Van Tol, E., Van Velzen-Williams, G. B. E. M., Overgauw, C. F., Ter Horst, H., Dekker, H., Okhuijsen, B., Seynen, M., Vijftigschild, A., Han, P., Katan, A. J., Schoots, K., Schumm, R., Van Loo, W., Oosterkamp, T. H., and Frenken, J. W. M. *Review of Scientific Instruments* **76**(5) (2005). Cited By (since 1996): 43.

[46] Tersoff, J. *Phys. Rev. B* **40**(17), 11990–11993 (1989).

[47] Chen, C. J. *Phys. Rev. Lett.* **65**(4), 448–451 (1990).

[48] Sacks, W. *Phys. Rev. B* **61**(11), 7656–7668 (2000).

[49] Drakova, D. *Reports on Progress in Physics* **64**(2), 205 (2001).

[50] Crommie, M. F., Lutz, C. P., and Eigler, D. M. *Phys. Rev. B* **48**(4), 2851–2854 (1993).

[51] Stipe, B. C., Rezaei, M. A., and Ho, W. *Science* **280**(5370), 1732–1735 (1998).

[52] Lu, X., Grobis, M., Khoo, K. H., Louie, S. G., and Crommie, M. F. *Phys. Rev. Lett.* **90**(9), 096802 (2003).

[53] Jdira, L., Liljeroth, P., Stoffels, E., Vanmaekelbergh, D., and Speller, S. *Phys. Rev. B* **73**(11), 115305 (2006).

[54] Sinsarp, A., Yamada, Y., Sasaki, M., and Yamamoto, S. *Japanese Journal of Applied Physics* **42**(Part 1, No. 7B), 4882–4886 (2003).

[55] Pascual, J. I., Corriol, C., Ceballos, G., Aldazabal, I., Rust, H.-P., Horn, K., Pitarke, J. M., Echenique, P. M., and Arnau, A. *Phys. Rev. B* **75**(16), 165326 (2007).

[56] Hansma, P. K. *Tunneling Spectroscopy:Capabilities, Applications, and New Techniques*. Springer; 1 edition, (1982).

[57] Heinrich, A. J., Gupta, J. A., Lutz, C. P., and Eigler, D. M. *Science* **306**(5695), 466–469 (2004).

[58] Hahn, J. R., Lee, H. J., and Ho, W. *Phys. Rev. Lett.* **85**(9), 1914–1917 (2000).

[59] Hahn, J. R. and Ho, W. *The Journal of Chemical Physics* **131**(4), 044706 (2009).

[60] Sprodowski, C., Mehlhorn, M., and Morgenstern, K. *Journal of Physics: Condensed Matter* **22**(26), 264005 (2010).

[61] Klein, J., Léger, A., Belin, M., Défourneau, D., and Sangster, M. J. L. *Phys. Rev. B* **7**(6), 2336–2348 (1973).

[62] Jdira, L., Overgaag, K., Stiufiuc, R., Grandidier, B., Delerue, C., Speller, S., and Vanmaekelbergh, D. *Phys. Rev. B* **77**(20), 205308 (2008).

[63] Hasegawa, Y. and Avouris, P. *Phys. Rev. Lett.* **71**(7), 1071–1074 (1993).

[64] Stroscio, J. A. and Eigler, D. M. *Science* **254**(5036), 1319–1326 (1991).

[65] Meyer, G. and Rieder, K.-H. *Surface Science* **377-379**, 1087 – 1093 (1997). European Conference on Surface Science.

[66] Meyer, G., Zöphel, S., and Rieder, K.-H. *Phys. Rev. Lett.* **77**(10), 2113–2116 (1996).

[67] Bartels, L., Meyer, G., and Rieder, K.-H. *Phys. Rev. Lett.* **79**(4), 697–700 (1997).

[68] Moresco, F., Meyer, G., Rieder, K.-H., Tang, H., Gourdon, A., and Joachim, C. *Applied Physics Letters* **78**(3), 306–308 (2001).

[69] Hla, S.-W., Braun, K.-F., Wassermann, B., and Rieder, K.-H. *Phys. Rev. Lett.* **93**(20), 208302 (2004).

[70] Hla, S. W., Kuhnle, A., Bartels, L., Meyer, G., and Rieder, K. H. *Surface Science* **454-456**, 1079 – 1084 (2000).

[71] Crommie, M. F., Lutz, C. P., and Eigler, D. M. *Science* **262**(5131), 218–220 (1993).

[72] Manoharan H. C., Lutz C.P., E. D. *Nature* **403**, 512–515 (2000).

[73] Lagoute, J., Nacci, C., and Fölsch, S. *Phys. Rev. Lett.* **98**(14), 146804 (2007).

[74] Fölsch, S., Hyldgaard, P., Koch, R., and Ploog, K. H. *Phys. Rev. Lett.* **92**(5), 056803 (2004).

[75] Stipe, B. C., Rezaei, M. A., and Ho, W. *Science* **279**(5358), 1907–1909 (1998).

[76] Stipe, B. C., Rezaei, M. A., and Ho, W. *Phys. Rev. Lett.* **81**(6), 1263–1266 (1998).

[77] Lastapis, M., Martin, M., Riedel, D., Hellner, L., Comtet, G., and Dujardin, G. *Science* **308**(5724), 1000–1003 (2005).

[78] Komeda, T., Kim, Y., Kawai, M., Persson, B. N. J., and Ueba, H. *Science* **295**(5562), 2055–2058 (2002).

[79] Stroscio, J. A., Tavazza, F., Crain, J. N., Celotta, R. J., and Chaka, A. M. *Science* **313**(5789), 948–951 (2006).

[80] Backus, E. H. G., Eichler, A., Kleyn, A. W., and Bonn, M. *Science* **310**(5755), 1790–1793 (2005).

[81] Bartels, L., Wang, F., Moller, D., Knoesel, E., and Heinz, T. F. *Science* **305**(5684), 648–651 (2004).

[82] Jewell, A. D., Tierney, H. L., Baber, A. E., Iski, E. V., Laha, M. M., and Sykes, E. C. H. *Journal of Physics: Condensed Matter* **22**(26), 264006 (2010).

[83] Tikhodeev, S. G. and Ueba, H. *Phys. Rev. Lett.* **102**(24), 246101 (2009).

[84] Manzano, C., Soe, W.-H., Wong, H. S., Ample, F., Gourdon, A., Chandrasekhar, N., and Joachim, C. *Nature Materials* **8**, 576 (2009).

[85] Parschau, M., Hug, H. J., Rieder, K.-H., and Ernst, K.-H. *Surface and Interface Analysis* **-**, – (2010).

[86] Lee, H. J. and Ho, W. *Science* **286**(5445), 1719–1722 (1999).

[87] Lin, R., Braun, K. F., Tang, H., Quaade, U. J., Krebs, F. C., Meyer, G., Joachim, C., Rieder, K. H., and Stokbro, K. *Surface Science* **477**(2-3), 198 – 208 (2001).

[88] Moresco, F., Meyer, G., Rieder, K.-H., Tang, H., Gourdon, A., and Joachim, C. *Phys. Rev. Lett.* **86**(4), 672–675 (2001).

[89] Braun, K.-F. and Hla, S.-W. *Phys. Rev. B* **75**(3), 033406 (2007).

[90] Ternes, M., Lutz, C. P., Hirjibehedin, C. F., Giessibl, F. J., and Heinrich, A. J. *Science* **319**(5866), 1066–1069 (2008).

[91] Eigler, D. M., Lutz, C. P., and Rudge, W. E. *Nature* **352**, 600–603 (1991).

[92] Bartels, L., Meyer, G., and Rieder, K.-H. *Applied Physics Letters* **71**(2), 213–215 (1997).

[93] Gao, S., Persson, M., and Lundqvist, B. I. *Phys. Rev. B* **55**(7), 4825–4836 (1997).

[94] Whitman, L. J., Stroscio, J. A., Dragoset, R. A., and Celotta, R. J. *Science* **251**(4998), 1206–1210 (1991).

[95] Rezaei, M. A., Stipe, B. C., and Ho, W. *The Journal of Chemical Physics* **110**(10), 4891–4896 (1999).

[96] Martel, R., Avouris, P., and Lyo, I.-W. *Science* **272**(5260), 385–388 (1996).

[97] Lafferty, J. M., editor. *Foundations of Vacuum Science and Technology.* Wiley-Interscience, (1998).

[98] Hablanian, M. H., editor. *High-vacuum technology (A practical guide), 2. edition.* Marcel Dekker Inc, (1997).

[99] Meyer, G. *Review of Scientific Instruments* **67**(8), 2960–2965 (1996).

[100] Behler, S., Rose, M. K., Dunphy, J. C., Ogletree, D. F., Salmeron, M., and Chapelier, C. *Review of Scientific Instruments* **68**(6), 2479–2485 (1997).

[101] Foley, E. T., Yoder, N. L., Guisinger, N. P., and Hersam, M. C. *Review of Scientific Instruments* **75**(12), 5280–5287 (2004).

[102] White, G. K. and Meeson, P. J. *Experimental Techniques in Low-Temperature Physics (Monographs on the Physics and Chemistry of Materials, 59), 4th Edition.* Oxford University Press, (2002).

[103] Weisend, J. G. *The Handbook Of Cryogenic Engineering.* CRC Press, (1998).

[104] Besocke, K. *Surface Science* **181**(1-2), 145 – 153 (1987).

[105] Frohn, J., Wolf, J. F., Besocke, K., and Teske, M. *Review of Scientific Instruments* **60**(6), 1200–1201 (1989).

[106] Pertaya, N., Braun, K.-F., and Rieder, K.-H. *Review of Scientific Instruments* **75**(8), 2608–2612 (2004).

[107] Binnig, G. and Smith, D. P. E. *Review of Scientific Instruments* **57**(8), 1688–1689 (1986).

[108] Chen, C. J. *Applied Physics Letters* **60**(1), 132–134 (1992).

[109] Moheimani, S. O. R. *Review of Scientific Instruments* **79**(7) (2008). Cited By (since 1996): 9.

[110] Morisson, R. *Grounding and Shielding Techniques; 4 Sub edition.* Wiley-Interscience, (1998).

[111] Horcas, I., Fernandez, R., Gomez-Rodriguez, J. M., Colchero, J., Gomez-Herrero, J., and Baro, A. M. *Review of Scientific Instruments* **78**(1), 013705 (2007).

[112] Cavallini, M. and Biscarini, F. *Review of Scientific Instruments* **71**(12), 4457–4460 (2000).

[113] Nam, A. J., Teren, A., Lusby, T. A., and Melmed, A. J. *Journal of Vacuum Science & Technology B: Microelectronics and Nanometer Structures* **13**(4), 1556–1559 (1995).

[114] Albonetti, C., Bergenti, I., Cavallini, M., Dediu, V., Massi, M., Moulin, J.-F., and Biscarini, F. *Review of Scientific Instruments* **73**(12), 4254–4256 (2002).

[115] Cricenti, A., Paparazzo, E., Scarselli, M. A., Moretto, L., and Selci, S. *Review of Scientific Instruments* **65**(5), 1558–1560 (1994).

[116] Oliva, A. I., G., A. R., Pena, J. L., Anguiano, E., and Aguilar, M. *Review of Scientific Instruments* **67**(5), 1917–1921 (1996).

[117] Bastiman, F., Cullis, A. G., Hopkinson, M., and Briston, K. J. *Journal of Vacuum Science & Technology B: Microelectronics and Nanometer Structures* **28**(2), 371–375 (2010).

[118] Cohen, Y. and Aurbach, D. *Review of Scientific Instruments* **70**(12), 4668–4675 (1999).

[119] Cavallini, M., Aloisi, G., and Guidelli, R. *Langmuir* **15**, 2993–2995 (1999).

[120] Ottaviano, L., Lozzi, L., and Santucci, S. *Review of Scientific Instruments* **74**(7), 3368–3378 (2003).

[121] Nakamura, Y., Mera, Y., and Maeda, K. *Review of Scientific Instruments* **70**(8), 3373–3376 (1999).

[122] Hockett, L. A. and Creager, S. E. *Review of Scientific Instruments* **64**(1), 263–264 (1993).

[123] Biegelsen, D. K., Ponce, F. A., Tramontana, J. C., and Koch, S. M. *Applied Physics Letters* **50**(11), 696–698 (1987).

[124] Ekvall, I., Wahlström, E., Claesson, D., Olin, H., and Olsson, E. *Measurement Science and Technology* **10**(1), 11 (1999).

[125] Hla, S.-W., Braun, K.-F., Iancu, V., and Deshpande, A. *Nano Letters* **4**(10), 1997–2001 (2004).

[126] Musket, R., McLean, W., Colmenares, C., Makowiecki, D., and Siekhaus, W. *Applications of Surface Science* **10**(2), 143 – 207 (1982).

[127] Gallon, T. and Matthew, J. *Review of Physics in Technology* **3**(1), 31 (1972).

[128] Heinz, K. *Reports on Progress in Physics* **58**(6), 637 (1995).

[129] Ross, K. J. and Sonntag, B. *Review of Scientific Instruments* **66**(9), 4409–4433 (1995).

[130] Ternes, M., Heinrich, A. J., and Schneider, W.-D. *Journal of Physics: Condensed Matter* **21**(5), 053001 (2009).

[131] Grochola, G., du Plessis, J., Snook, I. K., and Russo, S. P. *Surface Science* **591**(1-3), 32 – 37 (2005).

[132] Zhao, X., Perry, S. S., Horvath, J. D., and Gellman, A. J. *Surface Science* **563**(1-3), 217 – 224 (2004).

[133] Quaas, N., Wenderoth, M., and Ulbrich, R. G. *Surface Science* **550**(1-3), 57 – 64 (2004).

[134] Maurel, C., Abel, M., Koudia, M., Bocquet, F., and Porte, L. *Surface Science* **596**(1-3), 45 – 52 (2005).

[135] Cercellier, H., Didiot, C., Fagot-Revurat, Y., Kierren, B., Moreau, L., Malterre, D., and Reinert, F. *Phys. Rev. B* **73**(19), 195413 (2006).

[136] Goyhenex, C. *Surface Science* **600**(1), 15 – 22 (2006).

[137] Allongue, P., Cagnon, L., Gomes, C., Gündel, A., and Costa, V. *Surface Science* **557**(1-3), 41 – 56 (2004).

[138] Biener, M. M., Biener, J., Schalek, R., and Friend, C. M. *Surface Science* **594**(1-3), 221 – 230 (2005).

[139] Bergman, A., Nordström, L., Burlamaqui Klautau, A., Frota-Pessôa, S., and Eriksson, O. *Phys. Rev. B* **73**(17), 174434 (2006).

[140] Pietzsch, O., Okatov, S., Kubetzka, A., Bode, M., Heinze, S., Lichtenstein, A., and Wiesendanger, R. *Phys. Rev. Lett.* **96**(23), 237203 (2006).

[141] Ford, D. C., Xu, Y., and Mavrikakis, M. *Surface Science* **587**(3), 159 – 174 (2005).

[142] ya Ohno, S., Yagyuu, K., Nakatsuji, K., and Komori, F. *Surface Science* **547**(3), L871 – L876 (2003).

[143] Alemozafar, A. R. and Madix, R. J. *Surface Science* **587**(3), 193 – 204 (2005).

[144] Alemozafar, A. R., Guo, X.-C., and Madix, R. J. *Surface Science* **524**(1-3), L84 – L88 (2003).

[145] Kulawik, M., Rust, H.-P., Heyde, M., Nilius, N., Mantooth, B., Weiss, P., and Freund, H.-J. *Surface Science* **590**(2-3), L253 – L258 (2005).

[146] Lee, J., Lee, J.-G., Yates, J. T., and Jr. *Surface Science* **594**(1-3), 20 – 26 (2005).

[147] Neef, M. and Doll, K. *Surface Science* **600**(5), 1085 – 1092 (2006).

[148] Meyer, G., Zophel, S., and Rieder, K.-H. *Applied Physics Letters* **69**(21), 3185–3187 (1996).

[149] Stipe, B. C., Rezaei, M. A., and Ho, W. *Phys. Rev. Lett.* **82**(8), 1724–1727 (1999).

[150] Kim, Y., Komeda, T., and Kawai, M. *Phys. Rev. Lett.* **89**(12), 126104 (2002).

[151] Hallmark, V. M., Chiang, S., Brown, J. K., and Wöll, C. *Phys. Rev. Lett.* **66**(1), 48–51 (1991).

[152] Lagoute, J., Kanisawa, K., and Fölsch, S. *Phys. Rev. B* **70**(24), 245415 (2004).

[153] Hla, S.-W., Braun, K.-F., Wassermann, B., and Rieder, K.-H. *Phys. Rev. Lett.* **93**(20), 208302 (2004).

[154] Baro, A. M., Hla, S.-W., and Rieder, K. H. *Chemical Physics Letters* **369**(1-2), 240 – 247 (2003).

[155] Bohringer, M., Schneider, W. D., Göckler, K., Umbach, E., and Berndt, R. *Surface Science* **419**(1), L95 – L99 (1998).

[156] Gross, L., Moresco, F., Savio, L., Gourdon, A., Joachim, C., and Rieder, K.-H. *Phys. Rev. Lett.* **93**(5), 056103 (2004).

[157] Lu, X., Grobis, M., Khoo, K. H., Louie, S. G., and Crommie, M. F. *Phys. Rev. Lett.* **90**(9), 096802 (2003).

[158] Shi, D. X., Ji, W., Lin, X., He, X. B., Lian, J. C., Gao, L., Cai, J. M., Lin, H., Du, S. X., Lin, F., Seidel, C., Chi, L. F., Hofer, W. A., Fuchs, H., and Gao, H.-J. *Phys. Rev. Lett.* **96**(22), 226101 (2006).

[159] Gross, L., Rieder, K.-H., Moresco, F., Stojkovic, S. M., Gourdon, A., and Joachim, C. *nature materials* **4**, 892–895 (2005).

[160] Biener, M. M. and Friend, C. M. *Surface Science* **559**(2-3), L173 – L179 (2004).

[161] Hla, S. W., Marinkovic, V., and Prodan, A. *Surface Science* **356**(1-3), 130 – 136 (1996).

[162] Hla, S. W., Marinkovic, V., and Prodan, A. *Surface Science* **377-379**, 979 – 982 (1997). European Conference on Surface Science.

[163] Maurel, C., Ajustron, F., Péchou, R., Seine, G., and Coratger, R. *Surface Science* **600**(2), 442 – 447 (2006).

[164] Spiecker, E., Schmid, A. K., Minor, A. M., Dahmen, U., Hollensteiner, S., and Jäger, W. *Phys. Rev. Lett.* **96**(8), 086401 (2006).

[165] Hebenstreit, W., Redinger, J., Horozova, Z., Schmid, M., Podloucky, R., and Varga, P. *Surface Science* **424**(2-3), L321 – L328 (1999).

[166] Schintke, S., Messerli, S., Pivetta, M., Patthey, F. m. c., Libioulle, L., Stengel, M., De Vita, A., and Schneider, W.-D. *Phys. Rev. Lett.* **87**(27), 276801 (2001).

[167] Kulawik, M., Nilius, N., Rust, H.-P., and Freund, H.-J. *Phys. Rev. Lett.* **91**(25), 256101 (2003).

[168] Shockley, W. *Phys. Rev.* **56**(4), 317–323 (1939).

[169] Burgi, L., Petersen, L., Brune, H., and Kern, K. *Surface Science* **447**(1-3), L157 – L161 (2000).

[170] Heller, E. J., Crommie, M. F., Lutz, C. P., and Eigler, D. M. *Nature* **369**, 464–466 (1994).

[171] Højrup Hansen, K., Gottschalck, J., Petersen, L., Hammer, B., Lægsgaard, E., Besenbacher, F., and Stensgaard, I. *Phys. Rev. B* **63**(11), 115421 (2001).

[172] Weismann, A., Wenderoth, M., Lounis, S., Zahn, P., Quaas, N., Ulbrich, R. G., Dederichs, P. H., and Blugel, S. *Science* **323**(5918), 1190–1193 (2009).

[173] Crommie, M. F., Lutz, C. P., and Eigler, D. M. *Nature* **363**, 524–527 (1993).

[174] Stroscio, J. A. and Celotta, R. J. *Science* **306**(5694), 242–247 (2004).

[175] Repp, J., Meyer, G., Rieder, K.-H., and Hyldgaard, P. *Phys. Rev. Lett.* **91**(20), 206102 (2003).

[176] Borisov, A. G., Kazansky, A. K., and Gauyacq, J. P. *Phys. Rev. B* **65**(20), 205414 (2002).

[177] Li, J., Schneider, W.-D., Berndt, R., Bryant, O. R., and Crampin, S. *Phys. Rev. Lett.* **81**(20), 4464–4467 (1998).

[178] Kliewer, J., Berndt, R., Chulkov, E. V., Silkin, V. M., Echenique, P. M., and Crampin, S. *Science* **288**(5470), 1399–1402 (2000).

[179] Olsson, F. E., Persson, M., Borisov, A. G., Gauyacq, J.-P., Lagoute, J., and Fölsch, S. *Phys. Rev. Lett.* **93**(20), 206803 (2004).

[180] Rabe, A., Memmel, N., Steltenpohl, A., and Fauster, T. *Phys. Rev. Lett.* **73**(20), 2728–2731 (1994).

[181] Izquierdo, J., Vega, A., and Balbs, L. C. *Surface Science* **352-354**, 902 – 906 (1996). Proceedings of the 15th European Conference on Surface Science.

[182] Pedersen, M., Boenicke, I. A., Laegsgaard, E., Stensgaard, I., Ruban, A., Norskov, J. K., and Besenbacher, F. *Surface Science* **387**(1-3), 86 – 101 (1997).

[183] de la Figuera, J., Prieto, J. E., Ocal, C., and Miranda, R. *Phys. Rev. B* **47**(19), 13043–13046 (1993).

[184] Diekhöner, L., Schneider, M. A., Baranov, A. N., Stepanyuk, V. S., Bruno, P., and Kern, K. *Phys. Rev. Lett.* **90**(23), 236801 (2003).

[185] Goldman A., Dose V., B. G. *Phys. Rev. B.* **32**, 1971 (1985).

[186] Li, J., Schneider, W.-D., Berndt, R., and Delley, B. *Phys. Rev. Lett.* **80**(13), 2893–2896 (1998).

[187] Madhavan, V., Chen, W., Jamneala, T., Crommie, M. F., and Wingreen, N. S. *Science* **280**(5363), 567–569 (1998).

[188] Knorr, N., Schneider, M. A., Diekhöner, L., Wahl, P., and Kern, K. *Phys. Rev. Lett.* **88**(9), 096804 (2002).

[189] Argaman, N. and Makov, G. july (1999).

[190] Hohenberg, P. and Kohn, W. *Phys. Rev.* **136**(3B), B864–B871 (1964).

[191] Kohn, W. and Sham, L. J. *Phys. Rev.* **140**(4A), A1133–A1138 (1965).

[192] Vanderbilt, D. *Phys. Rev. B* **41**(11), 7892–7895 (1990).

[193] Perdew, J. P., Burke, K., and Ernzerhof, M. *Phys. Rev. Lett.* **77**(18), 3865–3868 (1996).

[194] Giannozzi, P., Baroni, S., Bonini, N., Calandra, M., Car, R., Cavazzoni, C., Ceresoli, D., Chiarotti, G. L., Cococcioni, M., Dabo, I., Corso, A. D., de Gironcoli, S., Fabris, S., Fratesi, G., Gebauer, R., Gerstmann, U., Gougoussis, C., Kokalj, A., Lazzeri, M., Martin-Samos, L., Marzari, N., Mauri, F., Mazzarello, R., Paolini, S., Pasquarello, A., Paulatto, L., Sbraccia, C., Scandolo, S., Sclauzero, G., Seitsonen, A. P., Smogunov, A., Umari, P., and Wentzcovitch, R. M. *Journal of Physics: Condensed Matter* **21**(39), 395502 (2009).

[195] Swartzentruber, B. S. *Phys. Rev. Lett.* **76**(3), 459–462 (1996).

[196] Naumovets, A. and Zhang, Z. *Surface Science* **500**(1-3), 414 – 436 (2002).

[197] Claytor, K., Khatua, S., Guerrero, J. M., Tcherniak, A., Tour, J. M., and Link, S. *The Journal of Chemical Physics* **130**(16), 164710 (2009).

Index of Figures

Appendix

Publications related to this thesis:

ZUPANIČ, Erik, ŽITKO, Rok, PRODAN, Albert, MUŠEVIČ, Igor. Načrtovanje in izdelava ultravisokovakuumskega kriostata s helijevo kopeljo za vrstično tunelsko mikroskopijo = Design and construction of an ultrahigh vacuum helium bath cryostat for scanning tunneling. *Vakuumist*, vol. **27** (1/2), 14-19 (2007).

ZUPANIČ, Erik, ŽITKO, Rok, MIDDEN, Herman J. P. van, MUŠEVIČ, Igor, PRODAN, Albert. Low-temperature scanning tunneling microscopy and spectroscopy of noble-metal surfaces. *Croat. Chem. Acta*, vol. **82** (2), 485-491 (2009).

ZUPANIČ, Erik, ŽITKO, Rok, MIDDEN, Herman J. P. van, MUŠEVIČ, Igor, PRODAN, Albert. Pinning of adsorbed cobalt atoms by defects embedded in copper (111) surface. *Phys. Rev. Lett.*, vol. **104** (19), 196102-1-196102-4 (2010).